Acta Pharmaceutica Sinica B 2025;15(11):6001−6018

Chinese Pharmaceutical Association
Institute of Materia Medica, Chinese Academy of Medical Sciences

Acta Pharmaceutica Sinica B

www.elsevier.com/locate/apsb
www.sciencedirect.com

ORIGINAL ARTICLE

Arsenic trioxide-based nanoparticles for enhanced chemotherapy by activating pyroptosis

Shengmei Wang[a,c], Ding Ma[e], Minghua Yang[f], Ye Zhang[f], Shengfeng Wang[a,*], Wenhu Zhou[b,d,g,*]

[a]*Department of Pharmacy, the third Xiangya Hospital, Central South University, Changsha, Hunan 410013, China*
[b]*Xiangya School of Pharmaceutical Sciences, Central South University, Changsha, Hunan 410013, China*
[c]*The First Hospital of Hunan University of Chinese Medicine, Changsha, Hunan 410007, China*
[d]*Key Laboratory of Biological Nanotechnology of National Health Commission, Changsha, Hunan 410008, China*
[e]*Department of Gastroenterology, the Third Xiangya Hospital, Central South University, Changsha, Hunan 410013, China*
[f]*Department of Pediatrics, the Third Xiangya Hospital, Central South University, Changsha, Hunan 410013, China*
[g]*Hunan Key Laboratory of the Research and Development of Novel Pharmaceutical Preparations, School of Pharmaceutical Science, Changsha Medical University, Changsha 410219, China*

Received 11 January 2025; received in revised form 25 March 2025; accepted 14 April 2025

KEY WORDS

Nanoparticles;
Cell death;
Chemotherapy;
Targeting;
Tumor immunity;
Drug delivery;
Arsenic trioxide;
Hepatocellular carcinoma

Abstract Chemotherapy remains a primary treatment option for hepatocellular carcinoma (HCC), yet its clinical benefits are often unsatisfactory. Utilizing arsenic trioxide (ATO) as a model, this study elucidates the role of autophagy inhibition in modulating the cellular response to chemotherapy, shifting cell death from apoptosis to pyroptosis *via* the caspase-3-GSDME pathway, thereby augmenting the antitumor efficacy. Building upon these findings, an ATO nanomedicine delivery system capable of autophagy inhibition to promote pyroptosis for enhanced tumor treatment was developed. Folic acid-modified albumin served as the stabilizer for nano self-assemblies formed through ion pairing between Mn^{2+} and ATO, encapsulating DNAzyme (Dz) targeting Beclin 1, a key autophagy regulator. Characterization studies confirmed efficient encapsulation of ATO and Dz within nanoparticles, designed to disintegrate in the intracellular microenvironment, releasing the all-active components, *i.e.*, ATO, Mn^{2+}, and Dz. Mn^{2+} acted as a metal cofactor to activate Dz for *Beclin* 1 mRNA cleavage, inhibiting autophagy and augmenting ATO-induced cell pyroptosis. Elevated cell pyroptosis levels not only enhance ATO's direct tumor cell killing capacity but also trigger anti-tumor immune responses, synergistically enhancing efficacy. Upon intravenous injection, the nanomedicine accumulated in tumor tissue and targeted liver cancer cells. Compared to free ATO, the nanomedicine exhibited significantly improved *in vivo* anti-tumor

*Corresponding authors.
E-mail addresses: zhouwenhuyaoji@163.com (Wenhu Zhou), sunfeelwang@csu.edu.cn (Shengfeng Wang).

Peer review under the responsibility of Chinese Pharmaceutical Association and Institute of Materia Medica, Chinese Academy of Medical Sciences.

https://doi.org/10.1016/j.apsb.2025.08.003

effects, achieving a 100% 45-day survival rate in mice with favorable biosafety profiles. This study offers novel insights into tumor chemotherapy sensitization and presents a promising strategy for ATO nanoformulation development.

1. Introduction

Liver cancer remains a significant global health concern, with approximately 0.86 million new cases reported annually, ranking as the third leading cause of cancer-related mortality[1,2]. Hepatocellular carcinoma (HCC) constitutes the predominant form of liver cancer, representing approximately 90% of cases, often diagnosed at advanced stages, resulting in unfavorable prognoses[3,4]. Conventional therapeutic modalities exhibit limited efficacy in advanced HCC cases, encountering challenges such as treatment resistance and adverse drug reactions, leading to stagnant overall survival rates over the past decade[5,6]. Consequently, there is an imperative to innovate novel therapeutic approaches to overcome existing treatment bottlenecks and enhance liver cancer management outcomes[7,8].

Chemotherapy represents a cornerstone in cancer treatment, primarily inducing cellular apoptosis *via* the caspase-3 pathway to exert anti-tumor effects. However, the emergence of chemoresistance mediated by tumor cells poses a formidable challenge, manifesting through various mechanisms such as the inhibition of intracellular caspase-3 activity and blockade of the caspase-3 signaling cascade[9,10]. Consequently, there is a burgeoning interest in exploring cell death mechanisms beyond apoptosis as sensitization strategies for chemotherapy[11−13]. Pyroptosis, a regulated form of programmed cell death mediated by members of the Gasdermin (GSDM) protein family, has garnered attention due to its high immunogenicity and potent inflammatory responses[14,15]. Pyroptosis not only directly eliminates tumor cells but also elicits robust anti-tumor immune reactions, thereby impeding tumor progression[16−18]. Recent investigations have unveiled caspase-3 as an upstream regulator of the GSDME protein, wherein its cleavage by caspase-3 transforms non-inflammatory cell apoptosis into pyroptosis[19,20]. Hence, the caspase-3/GSDME signaling axis represents a pivotal "switch" governing the equilibrium between tumor cell apoptosis and pyroptosis, offering a promising avenue for enhancing chemotherapy efficacy.

Autophagy emerges as a pivotal regulator influencing both cell apoptosis and pyroptosis. While chemotherapy-induced apoptosis activates the autophagy pathway, protective autophagy can confer resistance to apoptosis by eliminating damaged organelles or proteins[21,22]. On the other hand, heightened autophagy in solid tumors may impair the activation of the caspase-3−GSDME pathway, hampering pyroptosis induction[23,24]. Despite the significant impact of autophagy on cell death modalities, the intricate regulatory interplay between autophagy, apoptosis, and pyroptosis remains incompletely understood. Given its profound implications for tumorigenesis, autophagy represents a potential target for modulating the balance between these modes of cell demise, albeit underscoring a paucity of related investigations.

Arsenic trioxide (ATO), a traditional Chinese mineral medicine, has emerged as a frontline therapeutic agent for advanced HCC owing to its ability to promote liver cancer cell apoptosis *via* p53 activation[25,26]. Recent insights reveal ATO's capacity to induce immunogenic cell death, rendering "cold" tumors susceptible to immunotherapy[27,28]. Moreover, ATO elicits pyroptosis in GSDME-expressing HCC cells, highlighting its potential as an anti-tumor agent that promotes pyroptosis[29]. Nonetheless, clinical ATO application is hampered by challenges such as rapid renal clearance necessitating frequent administration and significant toxicities associated with systemic distribution[30,31]. Consequently, there is growing interest in developing targeted ATO delivery systems to mitigate these drawbacks[32−35]. Recently, a nanodiamond-based carrier has been developed for ATO delivery, which could augment its anti-tumor efficacy by the intrinsic activity of the nanodiamond to modulate autophagy[36]. Thus, nanomedicine-based delivery strategies not only enhance ATO's pharmacokinetic properties, but also fine-tune its cell death modality induction, offering enhanced efficacy and reduced toxicity.

In this study, we elucidate the negative regulatory relationship between autophagy and pyroptosis in liver cancer through bioinformatics analysis, and validate the modulatory role of autophagy in ATO-induced apoptosis/pyroptosis balance using Hepa1-6 liver cancer cells as a model. Suppression of autophagy could enhance ATO-induced pyroptosis, thereby augmenting anti-tumor efficacy. Capitalized on these facts, a metal salt precipitation-based ATO nanoformulation strategy has been developed (Scheme 1A), leveraging folate-modified albumin as a template to stabilize Mn^{2+}-ATO nanoprecipitates while encapsulating *Beclin1* mRNA-silencing DNAzyme (Dz). Such "one-pot method" is advantageous for facile preparation and high drug loading capacity. The nanosystem could target liver cancer cells post-intravenous administration by exploiting the enhanced permeability and retention (EPR) effect and folate-mediated receptor recognition (Scheme 1B). Upon intracellular uptake, the nanosystem releases ATO, Mn^{2+}, and Dz, with Mn^{2+} activating Dz *in situ* to cleave and silence *Beclin1* mRNA, thereby inhibiting autophagy and enhancing ATO-mediated pyroptosis. Cellular pyroptosis not only intensifies tumor cell killing but also modulates the tumor immune microenvironment, offering a synergistic therapeutic approach. This study underscores the pivotal role of autophagy in regulating apoptosis/pyroptosis balance, presenting a novel strategy to enhance chemotherapy efficacy. Moreover, the metal salt precipitation-based self-assembly strategy offers insights into developing innovative ATO formulations.

2. Materials and methods

2.1. Materials, cells, and animals

Folic acid (FA), dimethyl sulfoxide (DMSO), 1-ethyl-3-(3-dimethylaminopropyl) carbodiimide (EDC), dipotassium ethylene diamine tetraacetate (EDTA-2K) and *N*-hydroxysuccinimide (NHS) were purchased from Sinopharm Chemical

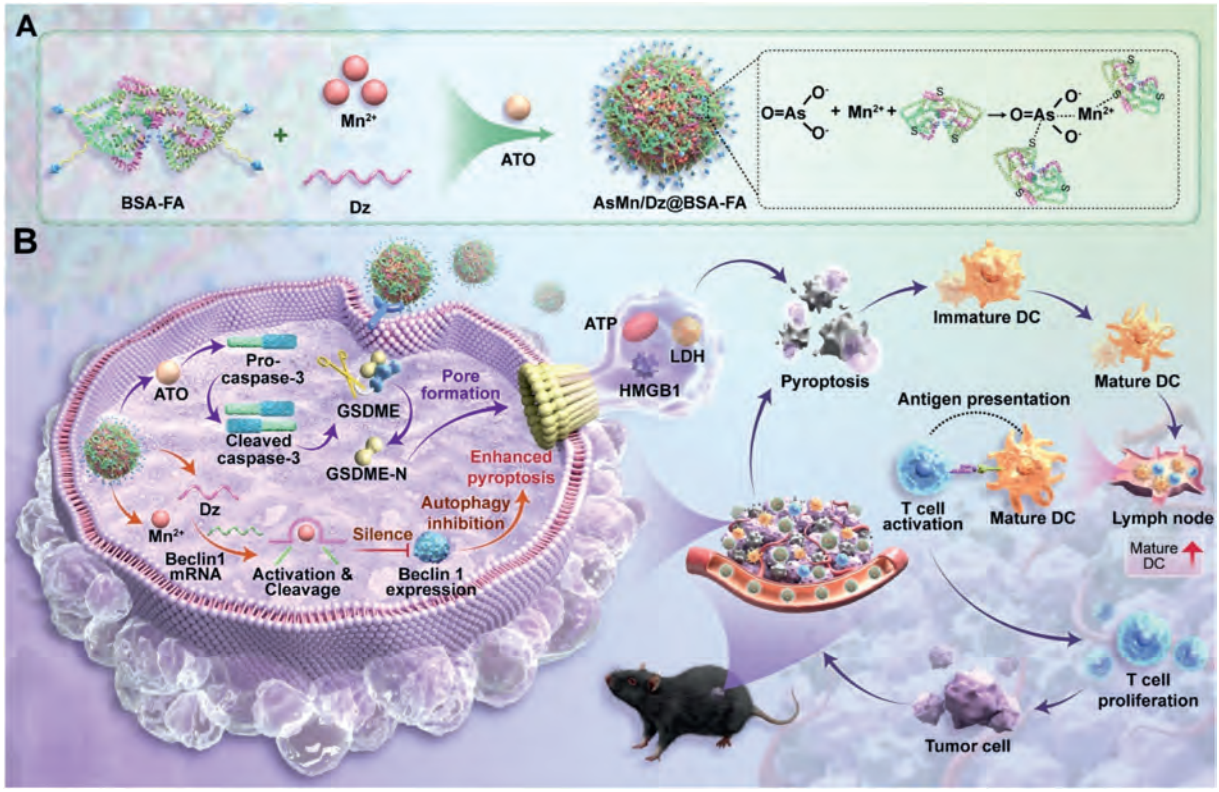

Scheme 1 Nanoparticle-mediated autophagy inhibition enhances arsenic trioxide chemotherapy in hepatocellular carcinoma by shifting cell death from apoptosis to pyroptosis. (A) Schematic showing the preparation process of AsMn/Dz@BSA-FA, and (B) the anti-tumor mechanisms of the nanomedicine.

Reagent Co., Ltd. (Shanghai, China). Beclin 1 DNAzyme (Dz), Cy5.5-labeled Beclin 1 DNAzyme (Dz-Cy5.5) and FAM-labeled Beclin 1 DNAzyme (Dz-FAM) (5′-TTCAATAAATGGC TCTCCGAGCCGGTCGAACTCCTGAGTTAGCCT-3′), and FAM-labeled substrate strand (5′-AGGCTAACTCAGGA-GrAGGAGCCATTTATTGAA-3′) were purchased from Sangon Biotech Co., Ltd. (Shanghai, China). Manganese chloride ($MnCl_2$) and Bovine serum albumin (BSA) were purchased from Aladdin Co., Ltd. (Shanghai, China). Reactive oxygen species inhibitor *N*-acetyl-L-cysteine (NAC) was from Ambeed (Shanghai, China). Penicillin-streptomycin solution and fetal bovine serum (FBS) were purchased from Gibco Life Technologies (Gaithersburg, MD, USA). Dulbecco's modified Eagle's medium (DMEM) and trypsin lysate were purchased from Procell Life Science & Technology (Wuhan, China). The Annexin V-FITC/PI double staining Kit was obtained from BestBio (Shanghai, China). Cell Counting Kit-8 (CCK-8) was obtained from Biosharp (Hefei, China). BCA protein quantification kits was obtained from Beyotime Institute of Biotechnology (Jiangsu, China). Urea was from BioFRoxx (Guangzhou, China). Ac-DEVD-CHO (DEVD, a caspase-3 inhibitor) was obtained from MACKLIN (Shanghai, China). ECL chemiluminescence detection kit was obtained from Biosharp (Hefei, China). The antibodies of p-JNK, P38 MAPK, HMGB1 and calreticulin polyclonal antibody were from Proteintech Group Inc. (Wuhan, China). The antibodies of GAPDH, GSDME, GSDME-N-terminal, CD4, CD86 and CD8 were from Affinity (Yangli, China). Caspase-3 antibody was from Cell Signaling Technology (Boston, USA). Mouse tumor necrosis factor α (TNF-α) ELISA kit, mouse interleukin 6 (IL-6) ELISA kit, mouse interleukin 1β (IL-1β) ELISA kit instruction and mouse high mobility group protein B1(HMGB1) were from MEIMIAN (Wuhan, China). APC Anti-Mouse CD11c Antibody, PE Anti-Mouse CD86 Antibody, FITC Anti-Mouse CD3 Antibody, APC Anti-Mouse CD4 Antibody, PE Anti-Mouse CD8a Antibody and Purified Anti-Mouse CD16/32 Antibody were from Elabscience (Wuhan, China).

2.1.1. Cells

Hepa1-6 cells were obtained from Meisen CTCC (Jinhua, China). AML12 cells were obtained from Procell Life Science & Technology (Wuhan, China). HepG2 cells and Bel-7402 cells were kindly provided by Prof. Pan Chen from The Affiliated Cancer Hospital of Xiangya School of Medicine, Central South University. The cells were cultured with 5% CO_2 at 37 °C using DMEM complete medium with 10% fetal bovine serum, 1% streptomycin and 1% penicillin.

2.1.2. Animals

C57BL/6 mice (4 to 6 weeks old) were obtained from Hunan SJA Laboratory Animal Co., Ltd. (Changsha, China). All experimental procedures were carried out in accordance with the plan approved by the Animal Protection and Use Committee of the Third Xiangya Hospital of Central South University (No. 2022-S307).

2.2. Single cell sequencing analysis to examine the correlation between autophagy and pyroptosis

The gene expression data from the GEO database (Gene Expression Omnibus, https://xenabrowser.net/datapages/) for liver cancer tissue samples and adjacent normal tissue samples were analyzed

using RNA sequencing (ID: GSE 149614) with the Seurat v3 method. Enrichment analysis was conducted to compare the expression of autophagy- and pyroptosis-related genes in normal liver tissues and tumor tissues.

2.3. Synergistic impact of autophagy inhibitors (CQ) and ATO

First, the cytotoxicity of Hepa1-6 cells was assessed at varying concentrations of ATO and ATO + CQ using the CCK-8 method. Subsequently, Hepa1-6 cells were seeded at a density of 2×10^5 cells/well in 6-well plates and divided into four groups: Control, CQ, ATO, and ATO + CQ intervention cells for a duration of 48 h. The cellular morphology of each group was observed under an optical microscope. The expression levels of Beclin 1, LC3, P62, GSDME, GSDME-N, caspase-3, p-JNK and P38 MAPK were analyzed through Western blotting (WB), with particular emphasis on verifying the combined effect of ATO and CQ. Furthermore, LDH release in different hepatoma cell lines (HepG2, Hepa1-6 and Bel-7402) following various treatments was determined using an LDH cytotoxicity assay kit. Annexin V-FITC/PI double staining was employed to analyze pyroptosis in Hepa1-6 cells after exposure to different treatment conditions. Finally, ROS production in Hepa1-6 cells treated with different preparations was analyzed by flow cytometry, while the rescue effect of NAC on ATO + CQ-induced cytotoxicity was assessed using the CCK-8 assay.

2.4. Transcriptome sequencing

Hepa1-6 cells were seeded in 6-well plates with 2×10^5 cells/well, incubated overnight, and then treated with Control, ATO and ATO + CQ for 48 h. After treatment, the cells were collected for transcriptome sequencing.

2.5. Preparation of the AsMn/Dz@BSA-FA

First, BSA-FA was synthesized using our previously established method[37]. Subsequently, a 200 μL solution of Dz was slowly added to the BSA-FA solution and stirred at 37 °C for 1 h. Following this, a 200 μL solution of $MnCl_2$ (50 mol/L) was added and stirred at 37 °C for 2 h. Then, a 200 μL ATO solution (100 mol/L) was introduced and stirred for an additional duration of 10 min before centrifuging at 17,800×*g* for 10 min to eliminate any unreacted BSA-FA and inorganic ions, resulting in the formation of AsMn/Dz@BSA-FA. To optimize the final concentrations of BSA (0.33, 0.67, 1, 1.33 and 1.67 mg/mL), $MnCl_2$ (4.17, 8.33, 16.67, 25 and 33.33 mol/L), as well as ATO (4.17, 8.33, 12.5 and 16.67 mol/L), we assessed the particle size and PDI values associated with each set of nanoparticles.

2.6. Screening of Dz

Hepa1-6 cells were seeded at a density of 2×10^5 cells/well in 6-well plates and incubated for 24 h. Subsequently, Lip3000-incubated Dz and Mn^{2+} were added to the cells. After a 6-h incubation, the culture medium was discarded, and the cells were washed with PBS before protein collection. The expression of Beclin 1 protein in each group was analyzed using WB.

2.7. Characterization of AsMn/Dz@BSA-FA

The particle size and ζ potential of nanoparticles were determined through dynamic light scattering (DLS) analysis using the Malvern Zetasizer Nano series (Nano ZS, Malvern instruments). The morphology and elemental distribution of AsMn/Dz@BSA-FA were observed *via* transmission electron microscopy-energy dispersion spectrometry (TEM-EDS, Titan G2 60-300, FEI). UV−Vis spectra of BSA, BSA-FA, FA, ATO, AsMn@BSA, and AsMn/Dz@BSA-FA were measured using a UV−Vis spectrophotometer. Inductively coupled plasma-optical emission spectrometry (ICP-OES) was employed to determine the drug loading capacity (LC%) and encapsulation efficiency (EE%) of ATO. In a darkroom, the verification of Dz (FAM-labeled) loading onto the nanoparticles was conducted by capturing fluorescence images under 470 nm LED excitation. To determine the loading capacity of Dz, AsMn/Dz@BSA-FA complexes were prepared using FAM-labeled Dz at varying concentrations (0.5, 1, 2, and 4 μmol/L). Following centrifugation at 17,800×*g* for 10 min, the unencapsulated Dz in the supernatant was collected and quantified through gel electrophoresis. The gel images were captured using a conventional camera. To investigate the colloidal stability, AsMn/Dz@BSA-FA was subjected to incubation in water, 10% FBS, and DMEM media supplemented with 10% FBS. The particle size was assessed at various time points including 0, 1, 2, 4, 8, and 24, and 48 h. Equilibrium dialysis was employed to investigate the *in vitro* release of AsMn/Dz@BSA-FA. A volume of 1 mL of AsMn/Dz@BSA-FA solution was introduced into a pre-treated dialysis bag, which was then placed inside a 50 mL centrifuge tube containing 19.0 mL of various release media. Samples were collected at specified time intervals (0, 0.5, 1, 2, 4, 6, 8, 12, and 24 h) and subsequently analyzed using ICP-OES to determine the drug concentration and calculate the cumulative release of ATO in each medium.

2.8. Stability analysis of AsMn/Dz@BSA-FA in serum

Free Dz or AsMn/Dz@BSA-FA was incubated with FBS (5%, 10%, or 20%) at 37 °C for 3 h, followed by denaturation of FBS through heating at 95 °C for 10 min. Subsequently, the samples were introduced into Tris buffer containing EDTA and urea to liberate the encapsulated Dz, and the extent of Dz degradation was assessed using gel electrophoresis.

2.9. Cleavage activity assay of Dz

The cleavage activity of Dz was assessed using gel electrophoresis. A mixture containing Dz (10 μmol/L), substrate chain (10 μmol/L, FAM-labeled), and metal ions at various concentrations (0, 0.1, 0.2, 0.5, and 1 mmol/L) was prepared in a 50 mmol/L MES buffer (pH 7.0) to initiate the reaction. After incubation for 1 h, the reaction was quenched by adding urea (8 mol/L), and the resulting cleaved substrate fragments were separated and analyzed using gel electrophoresis. For the self-activation experiment of Dz, AsMn/Dz@BSA-FA was incubated with GSH (10 mmol/L). Subsequently, it was mixed with a substrate concentration of 1 μmol/L at a temperature of 37 °C for 1 h followed by analysis of its lysis activity using similar methods as described above.

2.10. Cellular uptake

Hepa1-6 cells were seeded onto 6-well plates at a density of 2×10^5 cells/well. After treatment with various preparations for 4 h, the cells were washed three times with PBS, enzymatically digested and collected, and subsequently resuspended in PBS for quantitative analysis using flow cytometry. Additionally, confocal laser scanning microscopy (CLSM, LSM780 NLO, Zeiss, Germany) was employed to visualize cellular uptake in each experimental group. To investigate the mechanism of uptake, the cells were pre-treated with free FA at a concentration of 1 mmol/L for 1 h prior to incubation with the nanoparticles.

Hepa1-6 and AML12 cells were seeded onto 6-well plates at a density of 2×10^5 cells/well, treated with AsMn/Dz@BSA-FA for 4 h, washed three times with PBS to collect cells, and finally resuspended in PBS for flow cytometry analysis.

2.11. Lysosome escape of AsMn/Dz@BSA-FA

Hepa1-6 cells were inoculated in confocal dishes at a density of 5×10^4 cells per dish and incubated overnight. Subsequently, FAM-labeled AsMn/Dz@BSA-FA was added and incubated for 1 or 8 h. After washing with PBS 3 times, LysoTracker Red was added to stain the lysosome for 30 min, and DAPI (1 μg/mL) was added to stain the nucleus for 10 min. Finally, the colocalization of AsMn/Dz@BSA-FA with the lysosome was observed by CLSM.

2.12. In vitro cytotoxicity

Hepa1-6 cells were seeded in 96-well plates at a density of 5000 cells/well. Following incubation and adhesion, various concentrations of ATO, AsMn@BSA, AsMn/Dz@BSA, and AsMn/Dz@BSA-FA were added and incubated for 48 h. Subsequently, CCK-8 solution was introduced for an additional 2 h. Finally, the absorbance at 490 nm was measured using a microplate reader (TECAN) to determine cell viability. The cytotoxicity of AsMn/Dz@BSA-FA towards AML12 cells was assessed using the identical procedure.

2.13. WB

After treatment with various formulations, cells were collected and lysed using RIPA buffer. Following quantification by the BCA protein kit, proteins were isolated *via* gel electrophoresis and transferred onto a polyvinylidene fluoride (PVDF) membrane before being blocked with 5% skim milk. Primary antibodies against Beclin 1, LC3, P62, GSDME, GSDME-N, caspase-3, CD4, CD8, CD86, HMGB1 and GAPDH were then added and incubated overnight at 4 °C. Subsequently labeled secondary antibodies containing HRP were added and incubated for an hour at room temperature. Finally, protein bands were detected using a chemiluminescence imager (BioSpectrum 300; UVP).

2.14. Annexin V-FITC/PI double staining analysis

Hepa1-6 cells were seeded in 6-well plates at a density of 2×10^5 cells/well and cultured overnight. Subsequently, the cells were treated with various preparations for 48 h. After treatment, the cells were harvested, washed with PBS, and resuspended in PI and FITC-Annexin binding solution. Finally, flow cytometry was employed to analyze the cellular samples.

2.15. LDH and IL-1β release

Hepa1-6 cells were seeded in 96-well plates at a density of 5×10^3 cells/well overnight, followed by incubation with various preparations for 48 h. Subsequently, LDH levels were measured using an LDH kit, IL-1β was quantified using an IL-1β ELISA kit, and ATP released from the supernatant of each experimental group was performed using an ATP detection kit.

2.16. In vitro cell viability and LDH release after addition of DEVD

Hepa1-6 cells were seeded in 96-well plates at a density of 5×10^3 cells/well overnight. Subsequently, the cells were treated with various preparations supplemented with DEVD for 48 h. The control group was treated without DEVD. Cell viability of Hepa1-6 cells was assessed using the CCK-8 method to determine relative cell viability. LDH release in Hepa1-6 cells with and without DEVD was detected by LDH kit.

2.17. In vitro CRT expression

Hepa1-6 cells were seeded onto 6-well plates at a density of 2×10^5 cells/well and incubated overnight. Subsequently, the cells were treated with various preparations for 48 h. Following this treatment, anti-CRT was introduced to the cell culture and allowed to incubate for an additional hour. FITC-labeled rabbit secondary antibodies were then added and incubated for half an hour before analysis using flow cytometry techniques. At the same time, the expression level of CRT protein on the cell membrane was analyzed by WB.

2.18. In vitro HMGB1 release

Hepa1-6 cells were seeded in 6-well plates at a density of 2×10^5 cells/well and incubated overnight. Following a 48-h treatment with various preparations, the concentration of HMGB1 in the cell supernatant was quantified using an enzyme-linked immunosorbent assay (ELISA), while the protein expression level of HMGB1 was assessed by WB analysis.

2.19. In vitro BMDCs stimulation

Bone marrow-derived dendritic cells (BMDCs) were isolated from 8-week-old female mice according to the established protocol[38]. Hepa1-6 cells were seeded in the upper compartment of a Transwell pore plate, while the lower chamber was seeded with BMDCs and incubated overnight. After the cells were attached to the wall, the upper chamber containing Hepa1-6 cells was treated with various preparations. Simultaneously, it was co-incubated with lower BMDCs for 48 h. Subsequently, the DCs were stained with anti-CD86-PE and anti-MHC II-APC and then analyzed by flow cytometry to assess their level of maturity.

2.20. Biocompatibility of AsMn/Dz@BSA-FA

The biocompatibility of AsMn/Dz@BSA-FA was evaluated by assessing its hemolytic activity using H_2O as a positive control and 0.9% NaCl as a negative control. Erythrocytes (red blood cells, 2% (*v*/*v*)) were incubated with various concentrations of AsMn/Dz@BSA-FA at 37 °C for 3 h followed by centrifugation. Subsequently, the supernatant's absorbance at 540 nm was

measured using a microplate reader (TECAN) to determine the extent of hemolysis.

2.21. *In vivo antitumor efficacy*

To establish a liver cancer model, Hepa1-6 cells were harvested and resuspended in PBS (1×10^7 cells/mL). The cell suspension was then combined with an equal volume of Matrigel and subcutaneously injected into the right axilla of mice at a dosage of 100 μL/animal. To study the distribution of organisms, when the tumor volume reached approximately 200 mm^3, the tumor-bearing mice were intravenously administered with free Dz-Cy5.5, AsMn/Dz-Cy5.5@BSA or AsMn/Dz-Cy5.5@BSA-FA. Subsequently, the mice were imaged using the IVIS Lumina XRMS Series III system (PerkinElmer, Waltham, MA) at 1 and 24 h post-injection. Major organs and tumors were then extracted from the mice and imaged *ex vivo* for further analysis.

To assess the *in vivo* anti-tumor efficacy of nanoparticles, when the tumor volume reached approximately 100 mm^3, the mice were randomly allocated into five groups and administered intravenously with PBS, ATO, AsMn@BSA, AsMn/Dz@BSA, and AsMn/Dz@BSA-FA (ATO:1 mg/kg) on Days 0, 3, 6, and 9 respectively. Tumor volume was assessed every two days during treatment to generate a tumor growth curve. On Day 20, tumor tissue was collected for photography and weighing. Hematoxylin and eosin (H&E) staining was performed on the tumor tissues and major organs. The expression of GSDME, GSDME-N, caspase-3, Beclin1, LC3 and P62 proteins in tumor tissues was detected by WB. The weight fluctuations of the mice during treatment were recorded. Serum levels of alanine aminotransferase (ALT), creatinine (CRE), aspartate aminotransferase (AST), and urea nitrogen (BUN) were quantified using standardized assay kits. To assess the immune effect, flow cytometry was used to detect the activation of DCs and T cells in tumor tissue. The levels of IL-6 and TNF-α in mouse tumor tissues were measured using ELISA. The expression of CD86, CD4, and CD8 proteins within the tumor was analyzed *via* WB. Immunofluorescence was employed to evaluate the expression of immune-related proteins within the tumor.

2.22. *Survival rate analysis*

When the tumor volume reached approximately 100 mm^3, the mice were randomly divided into five groups and administered with PBS, ATO, AsMn@BSA, AsMn/Dz@BSA, and AsMn/Dz@BSA-FA *via* caudal vein on Days 0, 3, 6, and 9 respectively (ATO:1 mg/kg). The mice were continuously monitored for a period of 45 days following the initiation of treatment on Day 0. Mice with a tumor volume exceeding 2000 mm^3 were considered deceased. Ultimately, all surviving mice were euthanized.

2.23. *Statistical analysis*

The mean ± standard deviation (SD) was used to present all quantitative data. Student's *t*-test and one-way analysis of variance (ANOVA) were employed to assess the differences between two groups and among multiple groups, respectively. Statistical significance was considered when $P < 0.05$ ($^*P < 0.05$, $^{**}P < 0.01$, $^{***}P < 0.001$, $^{****}P < 0.0001$).

3. Results and discussions

3.1. *Inhibiting autophagy enhances ATO-induced cell pyroptosis in liver cancer*

To investigate the interplay between autophagy and pyroptosis, we conducted bioinformatics analysis assessing the expression of pyroptosis-related genes (*GSDME*, *GSDMD*) and autophagy markers (P62, LC3) in normal liver tissue and HCC tumor tissue. GSDME and GSDMD are pivotal mediators of inflammatory cell death, termed "cell pyroptosis executors", which are cleaved by caspases to generate N-terminal domains targeting cell membranes and inducing pyroptosis[39]. P62 serves as a selective autophagy substrate, with its expression inversely correlated with autophagy activity[40]. Our analysis revealed elevated expression levels of GSDME (DFNA5), GSDMD, and P62 (SQSTM1) in HCC tumor tissues compared to normal tissues (Supporting Information Fig. S1). Moreover, a positive correlation was observed between P62, GSDME, and GSDMD expression levels (Supporting Information Fig. S2), suggesting a negative regulatory relationship between autophagy and pyroptosis.

To validate these findings, we employed ATO to stimulate Hepa1-6 cells and monitored pyroptosis and autophagy levels. Previous studies have demonstrated ATO-induced upregulation of autophagy in tumor cells, contributing to enhanced drug resistance in solid tumors[41]. Conversely, inhibiting autophagy has been shown to potentiate the therapeutic efficacy of ATO in liver cancer[36]. We observed a concentration-dependent reduction in cell viability following ATO treatment (Fig. 1A), concomitant with induction of autophagy as evidenced by P62 downregulation (Fig. 1B). To modulate autophagy, we utilized the autophagy inhibitor chloroquine (CQ). Within the tested concentration range (5 μmol/L), CQ did not significantly impact cell viability (Supporting Information Fig. S3), yet markedly enhanced the antitumor activity of ATO, leading to a threefold decrease in IC_{50} values (Fig. 1C). Treatment with CQ effectively abrogated ATO-induced autophagy, evidenced by upregulated levels of LC3-I/II and P62 (Fig. 1B and Supporting Information Fig. S4), implicating autophagy inhibition in augmenting ATO-mediated cytotoxicity.

Subsequent morphological assessments revealed a notable increase in bubble-shaped cells indicative of pyroptosis following ATO + CQ treatment compared to ATO alone (Fig. 1D and Supporting Information Fig. S5). Quantitative analysis *via* Annexin V-FITC/ PI dual staining confirmed a significant augmentation of pyroptotic cells in the ATO + CQ group relative to ATO treatment alone (Fig. 1E and Supporting Information Fig. S6). Furthermore, measurement of lactate dehydrogenase (LDH) release, a marker of cell rupture and pyroptosis, demonstrated increased LDH levels upon ATO treatment, with a significant enhancement observed in the ATO + CQ group (Supporting Information Fig. S7). WB analysis showed that there was no significant change in GSDMD after ATO treatment, and the levels of cleaved caspase-3 and GSDME-N increased, indicating the activation of caspase-3/GSDME pathway after ATO treatment (Fig. 1F, Supporting Information Figs. S8 and S9). Remarkably, co-treatment with ATO and CQ further potentiated pyroptosis pathway activation, corroborating the synergistic effect of autophagy inhibition on ATO-induced cell pyroptosis.

To elucidate the correlation between autophagy and pyroptosis, RNA transcriptome sequencing was performed on Hepa1-6 cells treated with control, ATO, and ATO + CQ. Differential gene

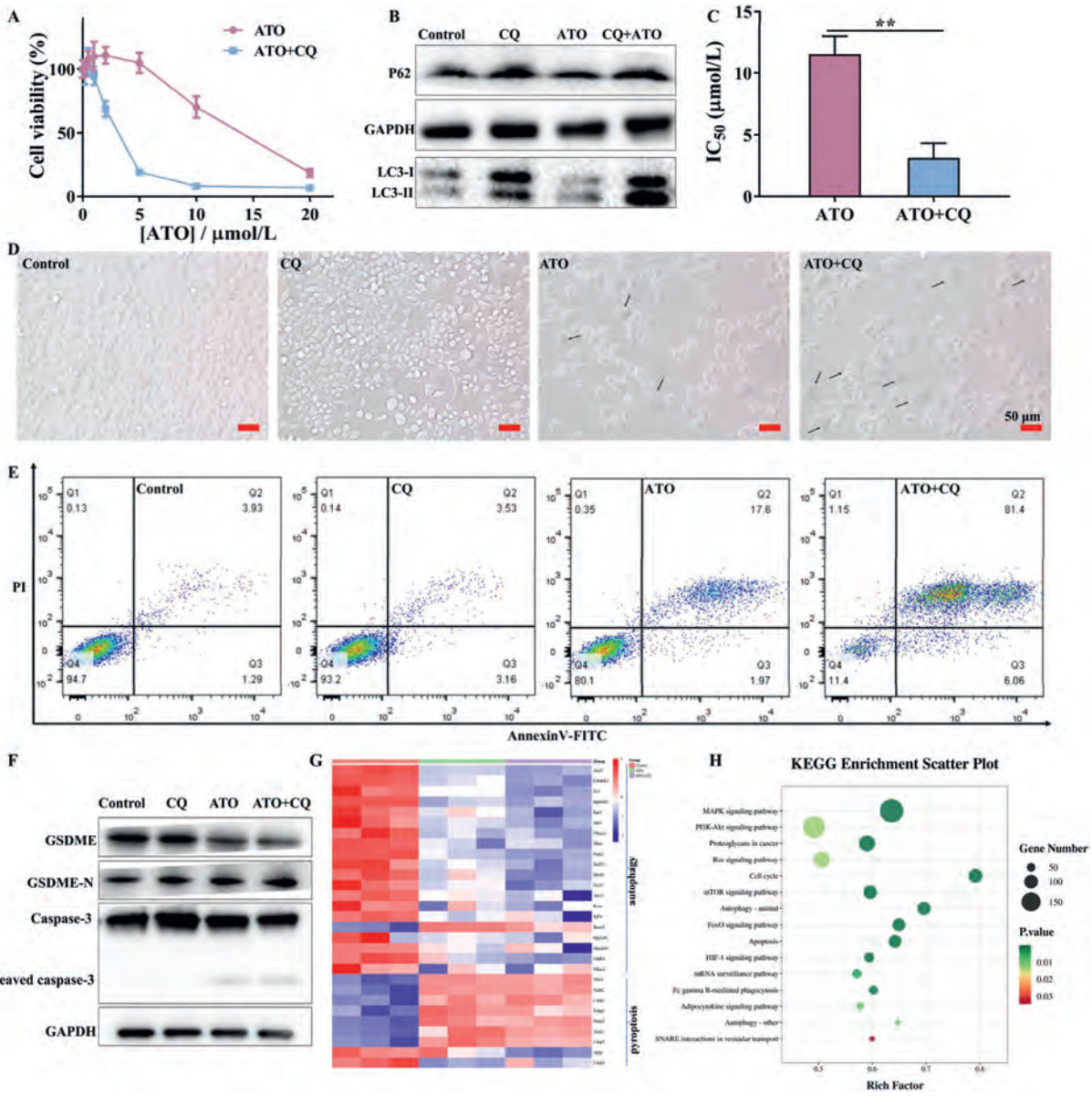

Figure 1 Synergistic effects of CQ and ATO. (A) Cell viability of Hepa1-6 cells treated with different concentrations of ATO and ATO + CQ for 48 h. (B) Expression of P62 and LC3 proteins after different treatments. (C) IC_{50} values of Hepa1-6 cells treated with different concentrations of ATO and ATO + CQ for 48 h. Data are presented as mean ± SD ($n = 3$). $^{**}P < 0.01$. (D) Cell morphology, Scale bar: 50 μm, (E) Annexin V/PI double staining analysis and quantification, and (F) expression of GSDEM, GSDEM-N, and caspase-3 proteins after different treatments. (G) Heat map of differentially expressed genes related to autophagy downregulation and pyroptosis upregulation. (H) KEGG pathway enrichment analysis of differentially expressed genes in Fig. 1G.

expression analysis revealed distinct gene expression profiles among the intervention groups, with the Venn plot highlighting differentially expressed and co-expressed genes (Supporting Information Fig. S10). Utilizing the Geecards database, we identified genes associated with both pyroptosis and autophagy, visualizing differentially expressed genes related to autophagy downregulation and pyroptosis upregulation *via* heat map visualization (Fig. 1G). Pathway enrichment analysis using the Kyoto Encyclopedia of Genes and Genomes (KEGG) database demonstrated enrichment of differentially expressed genes primarily in the MAPK signaling pathway (Fig. 1H). The MAPK pathway, comprising JNK and P38-MAPK branches, regulates Beclin-1 expression, a key autophagy promoter implicated in autophagosome formation[42]. Previous studies have implicated JNK and P38 MAPK in GSDME-dependent cell pyroptosis[43,44], suggesting their role in modulating the balance between autophagy and pyroptosis. Therefore, we further examined the protein expression levels of *p*-JNK and P38 MAPK *via* WB. The results demonstrated that, compared to the ATO group, the ATO + CQ group exhibited significantly increased phosphorylation of JNK and enhanced expression of P38 MAPK protein, suggesting that autophagy inhibition enhances pyroptosis *via* activation of the JNK/P38 MAPK signaling pathway (Supporting Information Fig. S11). As reported in the literature, ROS/JNK signaling cascade-mediated activation of caspase-3 can amplify pyroptosis[45]. To explore this, we further monitored the dynamic

changes in ROS levels following autophagy inhibition by CQ. The data showed that intracellular ROS levels in the ATO + CQ group were markedly elevated compared to the ATO and CQ monotherapy groups (Supporting Information Fig. S12A and S12B). To validate the role of ROS, we introduced the ROS inhibitor NAC, which significantly restored cell viability in the ATO + CQ group, confirming that ROS overaccumulation plays a crucial regulatory role in activating the GSDME-dependent pyroptosis pathway (Fig. S12C).

3.2. *Preparation and characterization of AsMn/Dz@BSA-FA*

The above results indicate that inhibiting autophagy can promote cell pyroptosis. However, autophagy inhibitor CQ is a lysosomal alkalizing agent, which can be affected by the acidic tumor microenvironment and entail toxicity concerns[46]. Therefore, modulating autophagy genetically may offer a more efficient and specific approach. We have previously designed a DNAzyme (Dz) capable of silencing *Beclin* 1 mRNA, effectively blocking autophagy (Supporting Information Fig. S13)[47]. Dz, a catalytic functional nucleic acid, can be activated by specific metal ion cofactors (*e.g.*, Mg^{2+}, Mn^{2+}, Zn^{2+}) to hydrolyze and cleave target mRNA, thus mediating gene silencing[48,49]. To this end, we developed a drug delivery system for co-delivery of ATO and anti-Beclin 1 Dz *via* a nanoprecipitation method. The specific process is illustrated in Scheme 1A, wherein bovine serum albumin (BSA) acts as a stabilizer, facilitating the formation of ATO insoluble salt with Mn^{2+} while encapsulating Dz to construct AsMn/Dz@BSA nanoparticles. Optimization of BSA, ATO, and Mn^{2+} concentrations based on particle size and polydispersity index (PDI) yielded final concentrations of 1 mg/mL, 8.33 mmol/L, and 4.17 mmol/L, respectively (Supporting Information Fig. S14). To further explore the combination of Mn^{2+} and ATO, we found that in the absence of BSA, ATO and Mn^{2+} spontaneously form a precipitate (AsMn), indicating a strong interaction and the formation of a stable complex. The addition of EDTA resulted in the dissolution of the precipitate, suggesting that the interaction between ATO and Mn^{2+} is based on metal coordination, and that EDTA chelates with Mn^{2+} or ATO, disrupting the AsMn structure (Supporting Information Fig. S15).

Quantitative assessment of Dz and calculation of encapsulation efficiency were conducted through fluorescence labeling of

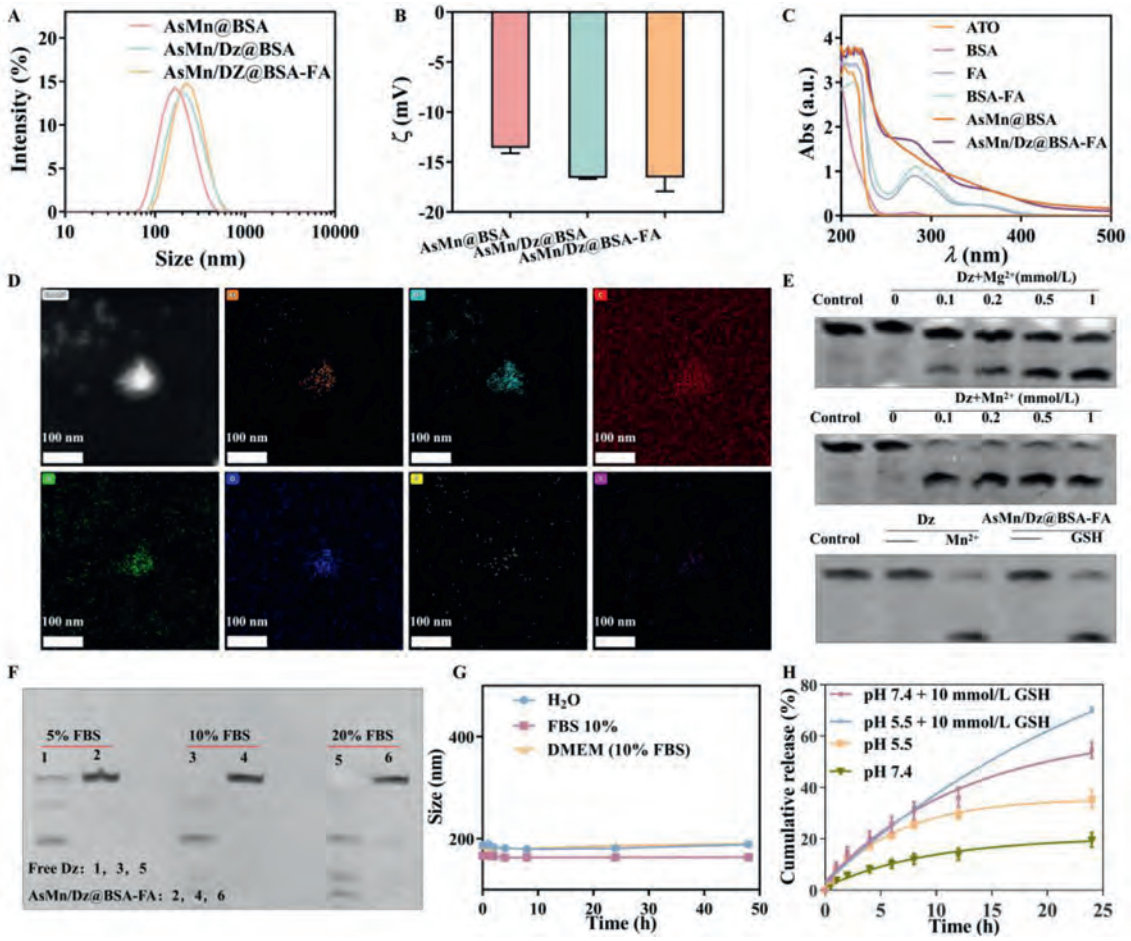

Figure 2 The characterizations of AsMn/Dz@BSA-FA. (A) Particle size characterization of each formulation, (B) ζ Potential, and (C) UV−Vis spectrum. (D) Elemental mapping of AsMn/Dz@BSA-FA nanoparticles. (E) Gel electrophoresis depicting Dz substrate cleavage under various conditions. (F) Gel electrophoresis showing the degradation of free Dz or Dz in AsMn/Dz@BSA-FA incubation with varying FBS concentrations. (G) Colloidal stability of AsMn/Dz@BSA-FA after 48 h of incubation in H_2O, 10% FBS, and DMEM cell culture medium (containing 10% FBS). (H) Drug release profiles of AsMn/Dz@BSA-FA under different conditions.

Dz. Encapsulation of Dz by nanoparticles was confirmed by a significant reduction in fluorescence signal compared to free Dz, indicating fluorescence quenching (Supporting Information Fig. S16). Additionally, gel electrophoresis quantitatively characterized the encapsulation efficiency, demonstrating efficient Dz encapsulation within the range of 0.5 to 4 μmol/L Dz feed concentrations (Supporting Information Fig. S17), attributed to strong metal ion-DNA coordination. Following Dz encapsulation, nanoparticles exhibited a slight increase in particle size and enhanced surface negativity (Fig. 2A and B). Quantification of ATO was achieved *via* ICP-OES, revealing drug loading and encapsulation efficiencies of 34.4% and 54.21%, respectively. To confer tumor-targeting properties to the nanostructure, folate-modified BSA (BSA-FA) was employed to fabricate targeted nanoparticles termed AsMn/Dz@BSA-FA. The characteristic absorption peaks of FA at 280 and 360 nm can be observed in BSA-FA *via* UV spectroscopy, and the BSA modified by FA changes from colorless to yellow, confirming the successful synthesis of BSA-FA (Fig. 2C and Supporting Information Fig. S18). Utilizing BSA-FA as a stabilizer, AsMn/Dz@BSA-FA nanoparticles exhibited a particle size of approximately 200 nm, a ξ potential of ~ -16 mV, with no significant differences compared to AsMn/Dz@BSA nanoparticles in terms of properties (Fig. 2A and B).

The TEM results indicated that AsMn/Dz@BSA-FA exhibit a stable, well-defined morphology, probably attributed to the presence of BSA on the surface (Supporting Information Fig. S19). The nanoparticle composition was characterized *via* Energy Dispersive X-ray Spectroscopy (EDS), revealing characteristic elemental peaks corresponding to As, P/N, and S of ATO, Dz, and BSA, alongside signals of Mn element (Fig. 2D). Mn^{2+} serves both as a structural component and a cofactor for Dz within the nanoparticles. To assess Dz catalytic activity in the presence of Mn^{2+}, we evaluated Dz cleavage under various conditions. While intracellular Mg^{2+} can also serve as a cofactor for Dz activation, its efficiency is comparatively lower. At physiological concentration (1 mmol/L), the cleavage rate after a 1-h reaction was only ~50%. However, the addition of Mn^{2+} significantly enhanced Dz cleavage activity, with an ~80% cleavage rate achieved under 0.1 mmol/L Mn^{2+} conditions (Fig. 2E). Notably, nanoparticles serve as Mn^{2+} reservoirs, releasing Mn^{2+} upon glutathione (GSH) treatment to achieve Dz self-activation, exerting a cleavage effect equivalent to free Mn^{2+}.

Biodegradation poses a significant challenge to *in vivo* application of Dz as a nucleic acid. Our previous studies have indicated that encapsulation of Dz in nanoparticles significantly enhances its stability[50–52]. To this end, we investigated the protective effect of AsMn/Dz@BSA-FA nanoparticles on Dz. Incubation of free Dz with FBS resulted in observable degradation bands in gel electrophoresis, with complete degradation observed in 20% FBS. In contrast, AsMn/Dz@BSA-FA nanoparticles exhibited minimal degradation, indicative of their protective effect on Dz (Fig. 2F). The colloidal stability and storage stability of nanoparticles were evaluated by monitoring the dynamic changes in particle size. There was no significant change in the particle size after 48 h of incubation in water, 10% fetal bovine serum, or DMEM cell culture medium containing 10% fetal bovine serum (Fig. 2G). Moreover, the nanoparticles maintained their size stability even after 15 days of storage at 4 °C (Supporting Information Fig. S20). Furthermore, *in vitro* drug release profiles demonstrated slow release under pH 7.4 conditions without burst release, facilitating prolonged drug circulation during *in vivo* delivery. Upon pH reduction to 5.5, drug release significantly accelerated, further enhanced upon GSH addition due to nanoparticle disintegration, facilitating intracellular drug release and Dz self-activation (Fig. 2H).

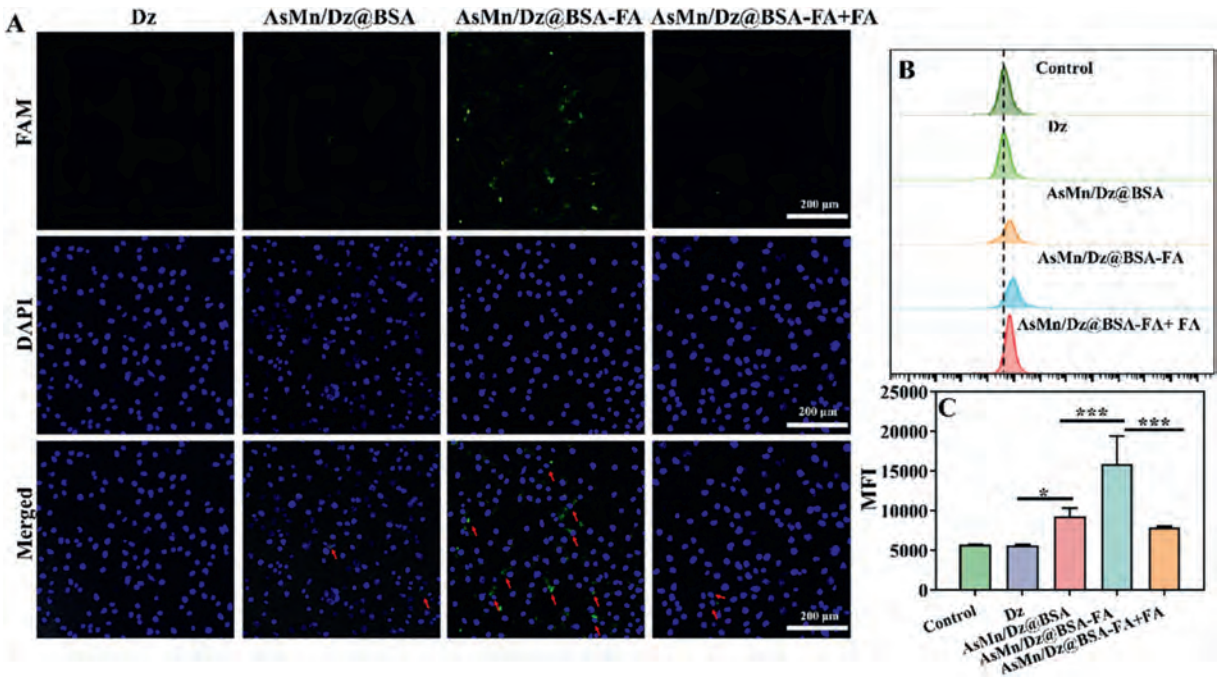

Figure 3 Cellular uptake of AsMn/Dz@BSA-FA. (A) CLSM images post-incubation of Hepa1-6 cells with different formulations. Scale bar: 200 μm. (B) Evaluation of cellular uptake of various formulations and their (C) quantitative analysis *via* flow cytometry. Data are presented as mean ± SD ($n = 3$). *$P < 0.05$, ***$P < 0.001$.

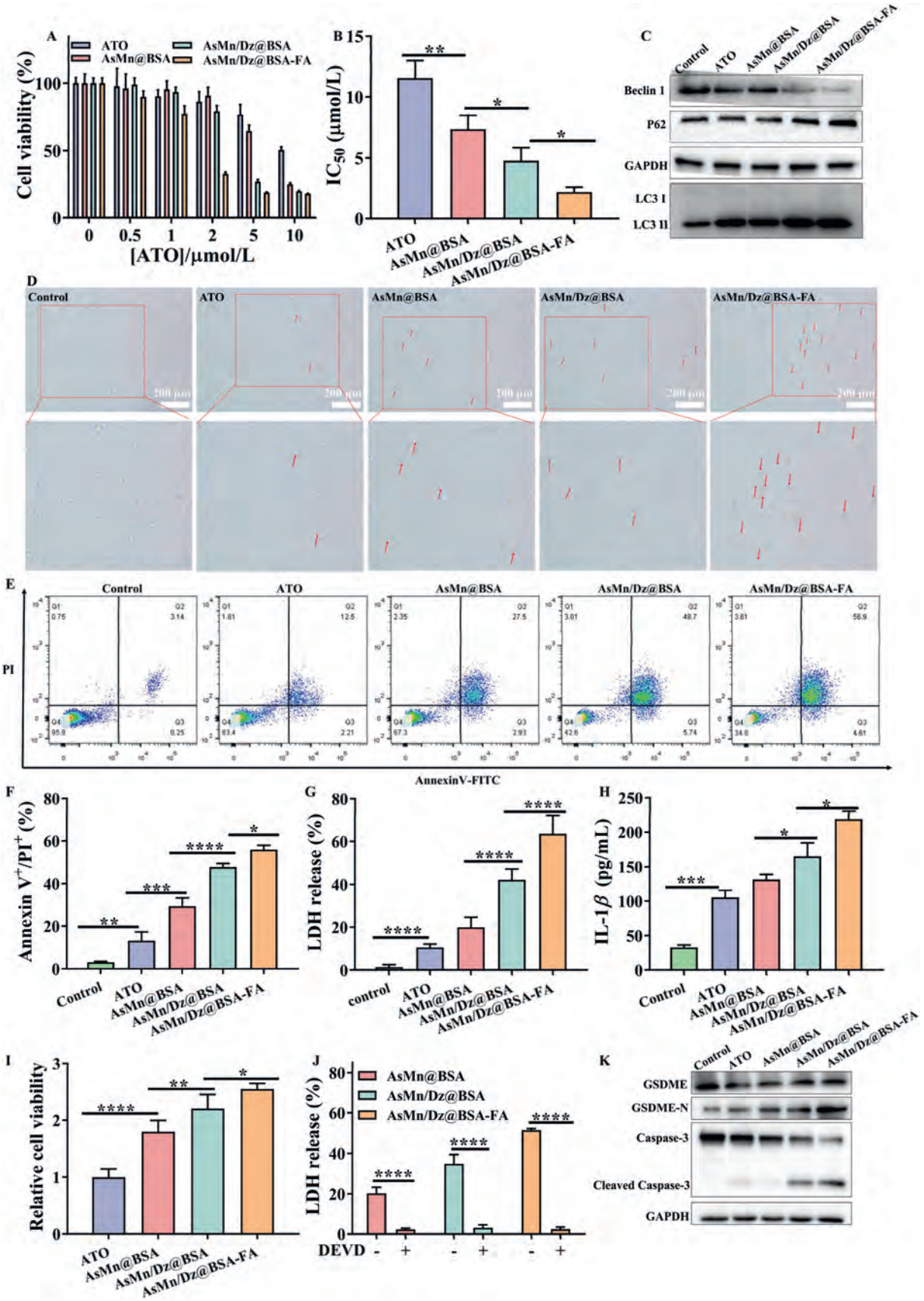

Figure 4 The *in vitro* antitumor effects and mechanisms of AsMn/Dz@BSA-FA. (A) Assessment of cell viability and (B) determination of IC_{50} values for various preparations incubated with Hepa1-6 cells for 48 h using the CCK-8 method. Data are presented as mean ± SD ($n = 3$).

3.3. *In vitro cell targeting characteristics of AsMn/Dz@BSA-FA*

Subsequently, we investigated the cellular uptake behavior of AsMn/Dz@BSA-FA nanoparticles, leveraging the active targeting properties conferred by folate modification within their structure. First, we determined the expression of folate receptor α (FRα) in Hepa1-6 cells and normal hepatocytes (AML12 cells) using ELISA. The results demonstrated that FRα expression in Hepa1-6 cells was significantly higher than that in normal hepatocytes (Supporting Information Fig. S21A). Therefore, the high FRα-expressing Hepa1-6 hepatocellular carcinoma cell model was selected to investigate the cellular uptake mechanism of the nanoparticles. To facilitate nanoparticle tracking, Dz was fluorescently labeled and observed using confocal laser scanning microscopy (CLSM) (Fig. 3A). Free Dz exhibited negligible intracellular fluorescence, while the AsMn/Dz@BSA group displayed only marginal fluorescence, indicative of limited cellular uptake. In contrast, the AsMn/Dz@BSA-FA group exhibited robust fluorescence signals, underscoring the efficacy of active targeted uptake. To further confirm folate receptor-mediated nanoparticle uptake, cells were pretreated with free FA to saturate folate receptor binding. Consequently, intracellular fluorescence in the AsMn/Dz@BSA-FA group was markedly diminished, corroborating the pivotal role of FA modification in targeted delivery. Subsequent quantification of fluorescence signals *via* flow cytometry (Fig. 3B and C) corroborated enhanced fluorescence intensity in the AsMn/Dz@BSA-FA group compared to the AsMn/Dz@BSA group, indicative of targeting capability. Notably, pretreatment with free FA attenuated AsMn/Dz@BSA-FA uptake efficiency to AsMn/Dz@BSA levels. To further validate the targeting specificity of AsMn/Dz@BSA-FA, the normal hepatocyte cell line AML12 was selected as a control. The results demonstrated that the cellular uptake of AsMn/Dz@BSA-FA was significantly higher in Hepa1-6 hepatocellular carcinoma cells compared to AML12 cells (Fig. S21B and S21C). Collectively, flow cytometry results aligned with CLSM observations, reaffirming targeted nanoparticle delivery to tumor cells facilitated by FA mediation. To track the transport of nanoparticles within the cells, lysosomes were co-stained with LysoTracker Red. The results showed minimal overlap between FAM (nanoparticles) and LysoTracker Red, indicating that most nanoparticles escaped from the lysosomes within 1 h (Supporting Information Fig. S22). With prolonged incubation, the green fluorescence increased due to greater nanoparticle internalization, while the co-localization with the red fluorescent lysosomes remained low. This confirms that ATO nanoparticles are efficiently delivered into cells, achieving lysosomal escape and the subsequent release of fully active components.

3.4. *In vitro anti-tumor effects of AsMn/Dz@BSA-FA*

Following the demonstration of tumor-targeted delivery, we proceeded to investigate the cytotoxic effects of nanoparticles on Hepa1-6 cells utilizing the CCK-8 method. After a 48-h incubation period, all formulations exhibited dose-dependent cytotoxicity (Fig. 4A), with subsequent calculation of IC_{50} values (Fig. 4B). Results indicate that AsMn@BSA displayed stronger cytotoxicity compared to free ATO, potentially attributed to enhanced cellular uptake of nanoparticles. Particularly noteworthy is the observation that encapsulation of Dz further potentiated the anti-tumor activity of nanoparticles, likely due to Dz's silencing effect on Beclin 1 protein. Notably, AsMn/Dz@BSA-FA demonstrated the most robust anti-tumor effect, underscoring the advantages of targeted nanoparticles.

Subsequently, we explored the mechanisms of the nanoformulation's anti-tumor effects. In our design, Dz-mediated silencing of Beclin 1 is leveraged to inhibit autophagy, thereby augmenting ATO's ability to induce cell pyroptosis. Initially, we assessed the expression of Beclin 1 across treatment groups. Compared to ATO and AsMn@BSA, both AsMn/Dz@BSA and AsMn/Dz@BSA-FA effectively silenced Beclin 1, with AsMn/Dz@BSA-FA exhibiting superior efficiency. *Beclin 1* silencing notably increased P62 protein and LC3-II expression, corroborating the inhibitory effect on cell autophagy (Fig. 4C and Supporting Information Fig. S23). To elucidate the induction potential of autophagy inhibition on cell pyroptosis, morphological changes in Hepa1-6 cells were observed using an inverted microscope (Fig. 4D). Post-AsMn/Dz@BSA-FA treatment, significant cellular swelling and the emergence of bubble-like structures were evident. Subsequent annexin V-FITC/PI double staining analysis, LDH release, and IL-1β measurements provided quantitative assessments of cell pyroptosis (Fig. 4E−H), with AsMn/Dz@BSA-FA exhibiting the highest pyroptosis induction.

To explore the cell pyroptosis pathway, the cells were pretreated with DEVD, a caspase-3 inhibitor. DEVD administration markedly attenuated the anti-tumor activity of each treatment group (Fig. 4I), with a notable reduction in LDH release (Fig. 4J). Notably, AsMn/Dz@BSA-FA demonstrated the most pronounced impact, indicating its reliance on the caspase-3 pathway for anti-tumor efficacy. Subsequent WB revealed elevated expression levels of cleaved caspase 3 and GSDME-N in Hepa1-6 cells post-treatment with Dz-loading nanoparticles, further affirming the pro-pyroptotic effect of Dz (Fig. 4K). Quantitative protein analysis underscored AsMn/Dz@BSA-FA's superior cell pyroptosis induction (Supporting Information Fig. S24). Additionally, nanoparticle toxicity on normal AML12 cells was investigated, with AsMn/Dz@BSA-FA exhibiting a 9-fold increase in Hepa1-6 cell IC_{50} compared to AML12 cells, highlighting nanoparticles' selective tumor cell killing ability (Supporting Information Fig. S25). This selectivity is attributed to both the high GSDME expression in tumor tissue, facilitating ATO-induced cell pyroptosis, and folate-mediated tumor-targeted delivery.

3.5. *Activation of anti-tumor immunity by AsMn/Dz@BSA-FA through promotion of cell pyroptosis*

Previous investigations have underscored the role of cell pyroptosis in enhancing exposure to tumor antigens, thereby

$^{*}P < 0.05$, $^{**}P < 0.01$. (C) Evaluation of LC3, Beclin1, and P62 protein expression in Hepa1-6 cells post-treatment with various preparations. (D) Morphological examination of Hepa1-6 cells following treatment with various preparations, Scale bar: 200 μm. (E, F) Analysis of Annexin V/PI double staining, (G) quantification of LDH release, and (H) measurement of IL-1β release in Hepa1-6 cells treated with various preparations. Data are presented as mean ± SD ($n = 3$). $^{*}P < 0.05$, $^{**}P < 0.01$, $^{***}P < 0.001$, $^{****}P < 0.0001$. Post-DEVD addition, (I) relative cell viability of Hepa1-6 cells and (J) LDH release in each formulation treatment group were evaluated. Data are presented as mean ± SD ($n = 4$). $^{*}P < 0.05$, $^{**}P < 0.01$, $^{****}P < 0.0001$. (K) Expression levels of GSDME, GSDME-N, and caspase-3 proteins after different treatments.

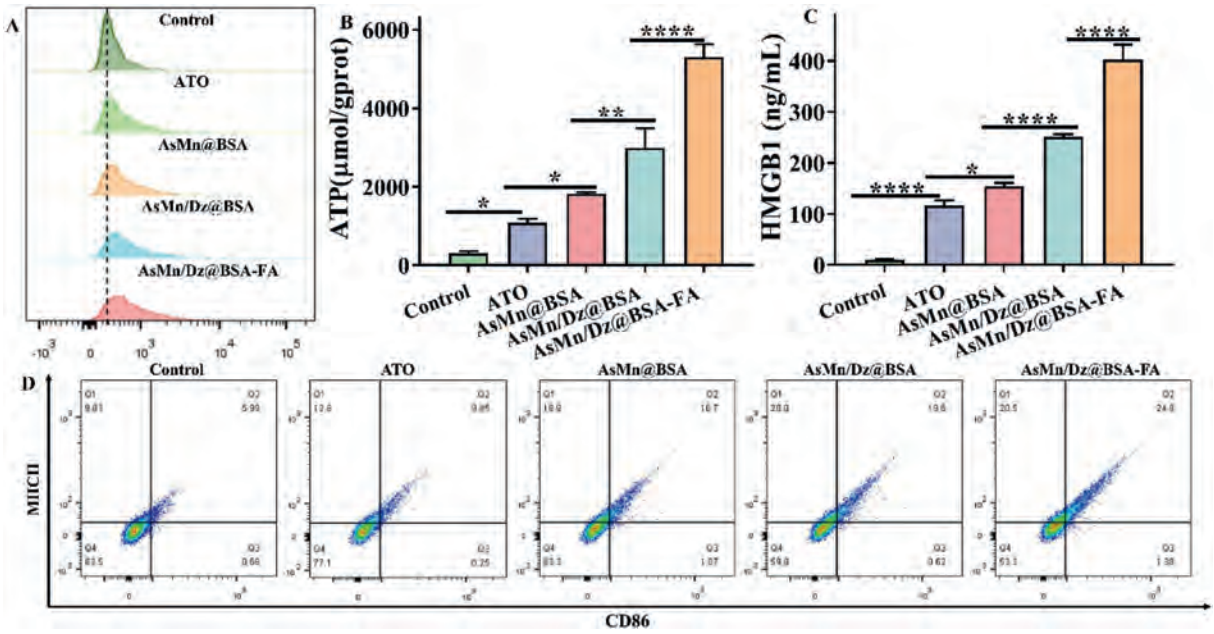

Figure 5 The immune response mediated by AsMn/Dz@BSA-FA *in vitro*. Exposure of (A) CRT and release of (B) ATP and (C) HMGB1 in Hepa1-6 cells treated with various formulations. (D) Proportions of BMDCs co-expressing CD86 and MHC II post-co-culture with Hepa1-6 cells treated with various formulations. Data are presented as mean ± SD ($n = 3$). *$P < 0.05$, **$P < 0.01$, ****$P < 0.0001$.

augmenting the tumor immune microenvironment and potentiating the efficacy of immunotherapy[53,54]. In light of this, we characterized the immunogenic cell death (ICD) of cells. Each treatment group exhibited heightened exposure to calreticulin protein (CRT) and released ATP and HMGB1 (Fig. 5A–C, Supporting Information Figs. S26 and S27). Notably, AsMn/Dz@BSA demonstrated stronger promotion of ICD compared to AsMn@BSA, indicative of the synergistic effect of Dz and ATO. The optimal effect was achieved with AsMn/Dz@BSA-FA, attributed to surface modification with folic acid. CRT exposure on the cell surface serves as an "eat me" signal to immune cells, facilitating dendritic cell (DC) maturation and phagocytosis of tumor cells[55]. Concurrently, HMGB1 and ATP release enhances tumor cell immunogenicity, recruiting immune cells, fostering immune cell differentiation and maturation, and thereby bolstering antigen-presenting activity[56–58]. Subsequently, co-culturing of Hepa1-6 cells treated with various formulations with mouse bone marrow-derived dendritic cells (BMDCs) allowed for *in vitro* analysis of DC maturation by assessing MHC II and CD86 co-stimulatory molecule expression using flow cytometry. Consistent with the above results, all formulations promoted DC antigen-presenting molecule and co-stimulatory molecule expression, with enhanced efficacy observed post-Dz encapsulation (Fig. 5D and Supporting Information Fig. S28). Thus, autophagy inhibition fosters cell pyroptosis, thereby augmenting tumor cell immunogenicity.

To validate this assertion, RNA sequencing analysis was conducted. Following ATO treatment, upregulation of genes related to inflammatory cytokines, antigen processing, and presentation was observed (Supporting Information Fig. S29A), pivotal in facilitating ICD. Moreover, autophagy inhibition intensified the induction effect of ICD. KEGG pathway enrichment analysis unveiled signaling pathways of differentially expressed genes post-autophagy inhibition, including "Intestinal immune network for IgA production", "Inflammatory mediator regulation of TRP channels", and "Cell adhesion molecules" (Fig. S29B), reaffirming the regulatory impact of autophagy inhibition on immune-related genes.

3.6. In vivo targeting and anti-tumor activity of AsMn/Dz@BSA-FA

Following the confirmation of nanoparticle functionality in cells, we further investigated their *in vivo* properties utilizing Hepa1-6 tumor-bearing mice. Preliminary blood compatibility experiments confirmed that within the concentration range of 1000 μg/mL, AsMn/Dz@BSA-FA exhibited a hemolysis rate of less than 2% (Supporting Information Fig. S30), rendering it suitable for intravenous injection. Initially, we examined the *in vivo* distribution of nanoparticles by labeling Dz with Cy5.5 fluorescence and employing small animal *in vivo* imaging techniques. After 1 h of intravenous injection, the nanoparticles exhibited widespread distribution throughout the body (Fig. 6A and Supporting Information Fig. S31). Over a 24-h period, the fluorescence signal notably decreased, indicative of nanoparticle metabolic elimination. Particularly noteworthy was the significant enhancement of nanoparticle fluorescence at the tumor site after 24 h, attributable to the enhanced permeability and retention (EPR) effect of the tumor. Subsequent *ex vivo* imaging and intensity quantification of main organs and tumor tissue validated these findings (Fig. 6B and C). Consistent with the aforementioned observations, nanoparticle intensity at the tumor site surpassed that of free Cy5.5, with folate-modified nanoparticles exhibiting optimal tumor-targeting enrichment, approximately 3.6 times higher than the fluorescence signal of free Cy5.5. These results underscore the active targeting properties of AsMn/Dz@BSA-FA, which benefits for enhancing drug anti-tumor efficacy and mitigating toxic side effects.

Having established tumor-targeted nanoparticle delivery, we then evaluated the *in vivo* anti-tumor efficacy of AsMn/Dz@BSA-

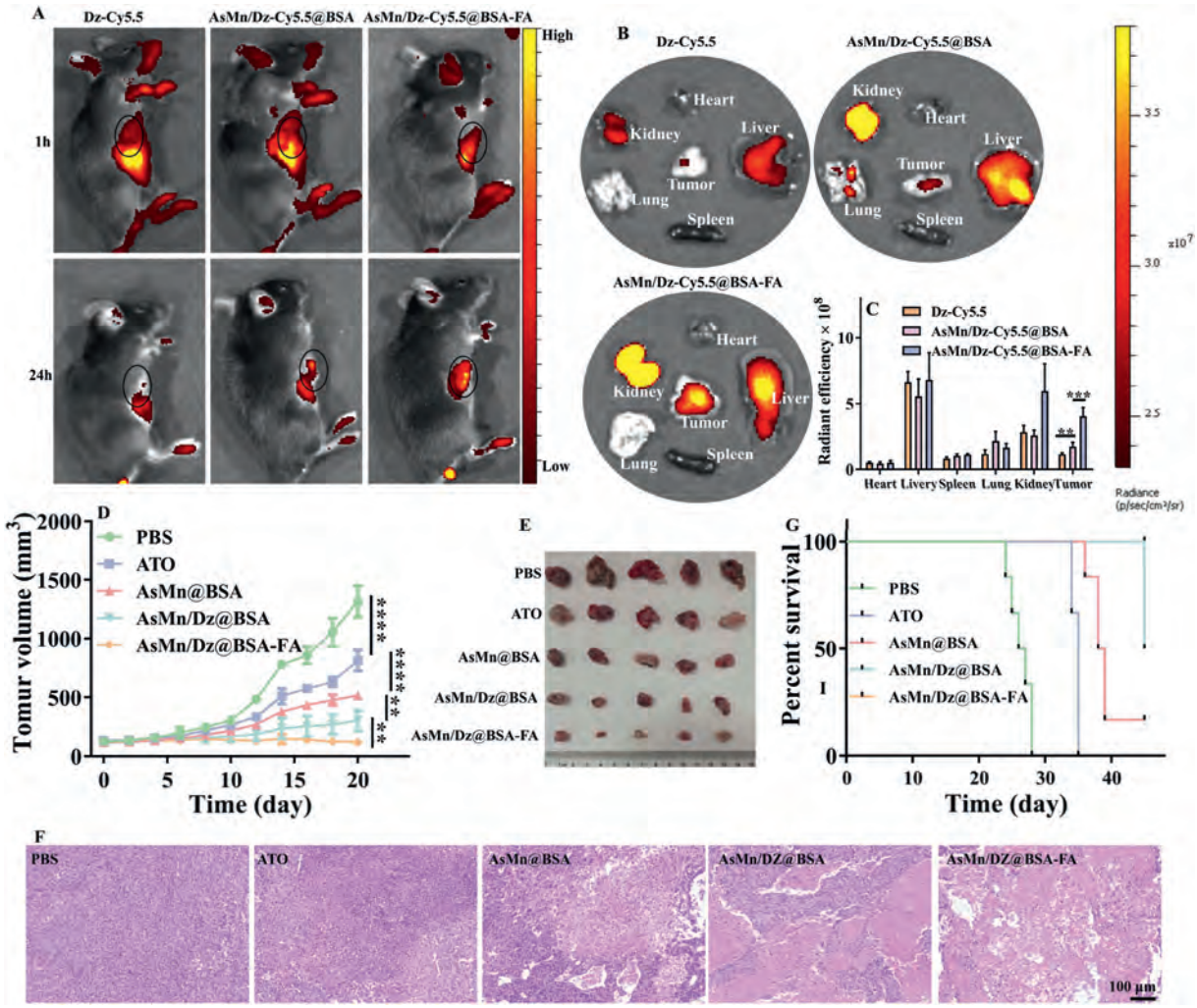

Figure 6 The biodistribution and antitumor activity of AsMn/Dz@BSA-FA *in vivo*. (A) *In vivo* and (B) *ex vivo* fluorescence images of tumor-bearing mice treated with various formulations, along with (C) fluorescence quantification. Data are presented as mean ± SD ($n = 3$). $^{**}P < 0.01$, $^{***}P < 0.001$. (D) Tumor growth curves of mice treated with various formulations. Data are presented as mean ± SD ($n = 5$). $^{**}P < 0.01$, $^{****}P < 0.0001$. (E) Visual images of tumors in each group at the end of treatment. (F) H&E staining for pathological evaluation of tumor tissue, Scale bar: 100 μm. (G) Survival rate of mice treated with various formulations ($n = 6$).

FA. Tumor-bearing mice were randomly divided into five groups and administered different formulations every three days for a total of four injections. Tumor tissue was measured every two days to assess anti-tumor effects. Moderate inhibition of tumor growth was observed with free ATO, while AsMn@BSA exhibited superior tumor inhibition, attributed to the tumor enrichment effect of nanoparticles. Incorporation of Dz nanoparticles further augmented tumor growth inhibition, indicative of the synergistic effect of Dz with ATO. Following folate modification, AsMn/Dz@BSA-FA demonstrated the most potent anti-tumor effect, nearly completely inhibiting tumor growth (Fig. 6D and Supporting Information Fig. S32). Direct evaluation of anti-tumor efficacy *via* measurement of tumor weight corroborated these findings (Fig. 6E and Supporting Information Fig. S33), with AsMn/Dz@BSA-FA exhibiting the most pronounced anti-tumor effect, followed by AsMn/Dz@BSA, AsMn@BSA, and free ATO. Pathological evaluation of tumor tissue *via* H&E staining revealed marked cell necrosis and nuclear reduction in the AsMn/Dz@BSA-FA group, underscoring its exceptional anti-tumor efficacy (Fig. 6F). Survival experiments on tumor-bearing mice further underscored the long-term efficacy of nanoparticles, with AsMn/Dz@BSA-FA-treated mice exhibiting a 100% survival rate at 45 days, significantly higher than other treatment groups, thus confirming the synergistic anti-tumor effect of Dz and ATO (Fig. 6G).

3.7. Validation of the in vivo anti-tumor mechanism of AsMn/Dz@BSA-FA

Encouraged by the outstanding *in vivo* anti-tumor efficacy of AsMn/Dz@BSA-FA, we further elucidated its underlying anti-tumor mechanism *in vivo*. In our design, the release of Mn^{2+} and Dz by nanoparticles within cells inhibits autophagy by catalyzing the cleavage of Beclin 1 protein, thereby promoting cell pyroptosis. Tumor cell pyroptosis subsequently releases tumor antigens, modulates the tumor immune microenvironment, and activates anti-tumor immunity. We validated these mechanisms *in vivo*. Compared to AsMn@BSA, AsMn/Dz@BSA, and AsMn/

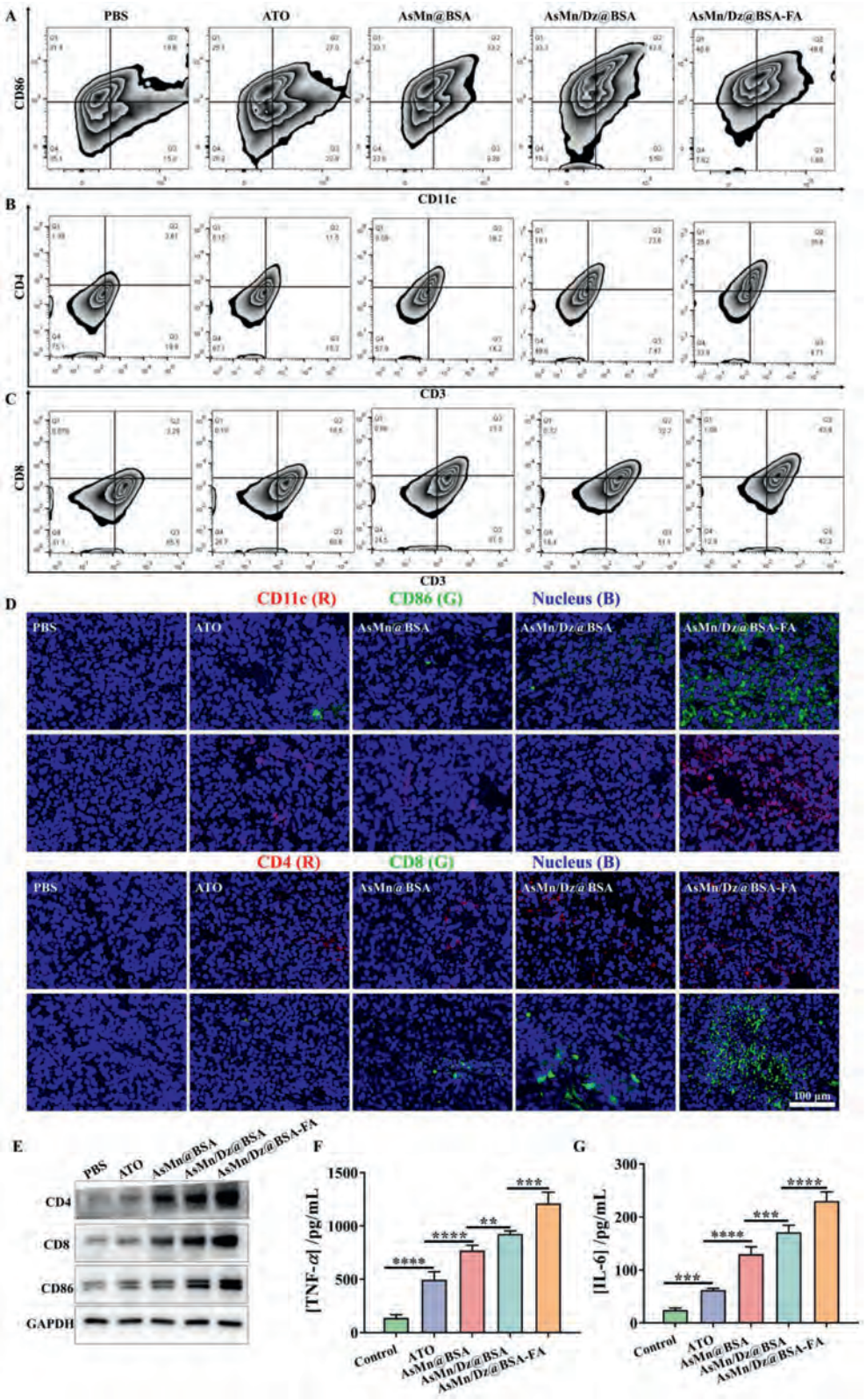

Figure 7 Immunomodulatory effects of AsMn/Dz@BSA-FA. Analysis of the proportion of (A) $CD11c^{+}CD86^{+}$ cells, (B) $CD3^{+}CD4^{+}$ cells, and (C) $CD3^{+}CD8^{+}$ cells in tumor tissues of each group of mice using flow cytometry. (D) Immunofluorescence detection of changes in CD86, CD11c, CD8, and CD4 in tumor tissue after treatment with different formulations, Scale bar: 100 μm. (E) Expression levels of CD86, CD8, and CD4 in tumor tissue after treatment with different formulations. Changes in (F) TNF-α and (G)IL-6 levels in tumor tissue after treatment with different formulations. Data are presented as mean ± SD ($n = 5$). $^{**}P < 0.01$, $^{***}P < 0.001$, $^{****}P < 0.0001$.

Dz@BSA-FA significantly downregulated the expression of Beclin 1 protein (Supporting Information Fig. S34A and S34B), confirming intracellular Dz activation and its mRNA-targeting silencing effect. Subsequent Beclin 1 protein silencing led to significant upregulation of LC3 and P62 (Figs. S34A, S34C, and S34D), confirming autophagy inhibition. Concurrently, the expression of cleaved caspase-3 and GSDME-N in tumors also increased (Fig. S34E−S34G), with AsMn/Dz@BSA-FA exhibiting the most pronounced regulatory effect. This underscores AsMn/Dz@BSA-FA's capacity to enhance cell pyroptosis by inhibiting autophagy, thereby achieving a synergistic effect of Dz and ATO.

Subsequently, we investigated the activation effect of cell pyroptosis on anti-tumor immunity, evaluating mature dendritic cells (mDCs) and tumor-infiltrating T cells through flow cytometry analysis. Compared with the control group, the proportion of activated DC cells ($CD86^+CD11c^+$) in tumor tissue significantly increased after treatment with AsMn/Dz@BSA and AsMn/Dz@BSA-FA, positively correlating with the level of cell pyroptosis (Fig. 7A, Supporting Information Figs. S35 and S36). Since DCs are essential for antigen presentation to T cells, their enhanced maturation indicates that AsMn/Dz@BSA-FA effectively overcomes the immunosuppressive TME by priming an antigen-specific immune response. We then examined T cell infiltration, and the results showed that AsMn/Dz@BSA-FA treatment led to a substantial increase in tumor-infiltrating cytotoxic T lymphocytes (CTLs, $CD3^+CD8^+$) and helper T cells (Ths, $CD3^+CD4^+$) (Fig. 7B and C, Figs. S35 and S36). This demonstrates that pyroptosis not only directly kills tumor cells but also fosters a pro-inflammatory TME conducive to T-cell recruitment and activation. Additionally, immunofluorescence assays confirmed significant enhancement of CD86, CD11c, CD4, and CD8 expression in tumor tissue after AsMn/Dz@BSA-FA treatment (Fig. 7D and Supporting Information Fig. S37). WB analysis of related proteins CD86, CD4, and CD8 corroborated the results obtained from immunofluorescence assays (Fig. 7E and Supporting Information Fig. S38), indicating initiation of an adaptive immune response by AsMn/Dz@BSA-FA treatment. Additionally, activated T cells secrete pro-inflammatory cytokines such as TNF-α and IL-6, which play crucial roles in sustaining

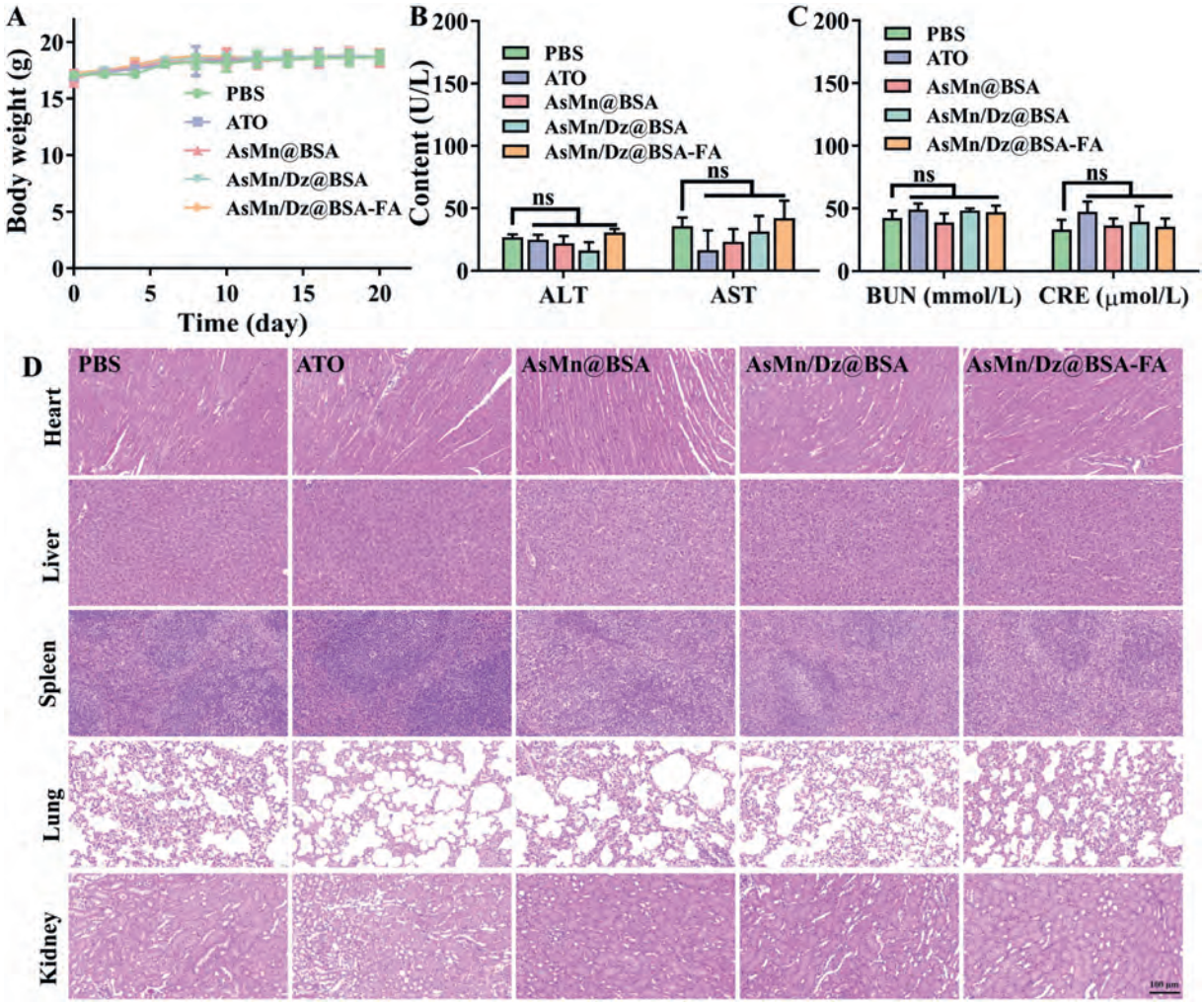

Figure 8 The biosafety of AsMn/Dz@BSA-FA *in vivo*. (A) Dynamic monitoring of weight changes during treatment. Evaluation of (B) hepatotoxicity and (C) nephrotoxicity of each formulation by measuring serum levels of ALT, AST, BUN, and CRE after treatment. Data are presented as mean ± SD ($n = 4$). ns, not significant. (D) Representative H&E staining images of major organs including the heart, liver, spleen, lungs, and kidneys after treatment with different formulations, Scale bar: 100 μm.

antitumor immunity. Consistent with this, ELISA assays revealed significantly higher levels of TNF-α and IL-6 in AsMn/Dz@BSA-FA-treated tumors (Fig. 7F and G). These cytokines contribute to direct tumor cell killing while further amplifying immune activation, reinforcing the antitumor response. Therefore, AsMn/Dz@BSA-FA not only induced tumor cell pyroptosis to directly eliminate tumors, but also achieved anti-tumor immunotherapy by promoting DC maturation, initiating T cell infiltration and activation, and cytokines excretion.

3.8. Biosafety assessment of AsMn/Dz@BSA-FA

Given the remarkable therapeutic effects observed, we conducted a thorough evaluation of the biosafety of the nanosystem. Throughout the treatment period, no significant fluctuations in body weight were observed, indicating the absence of acute toxicity associated with the different dosage forms (Fig. 8A). Furthermore, we assessed blood biochemical indicators including aspartate transaminase (AST), alanine transaminase (ALT), blood urea nitrogen (BUN), and creatinine (CRE) levels after treatment (Fig. 8B and C). The levels of these parameters remained within the normal range, suggesting the absence of hepatotoxicity or nephrotoxicity associated with each treatment. To comprehensively investigate systemic toxicity, we conducted histological examination *via* H&E staining of major organs (Fig. 8D). No pathological changes were observed in the heart, liver, spleen, lungs, or kidneys following treatment with any of the formulations. These findings collectively affirm the biocompatibility of the nanosystems for *in vivo* applications.

4. Conclusions

In conclusion, our study elucidated the intricate interplay between autophagy, apoptosis, and pyroptosis in HCC cells, revealing a negative correlation between autophagy and pyroptosis. By inhibiting autophagy, we successfully redirected ATO-induced cell death from apoptosis to pyroptosis, thus enhancing its anti-tumor effects. Leveraging these insights, we engineered a nanomedicine comprising ATO, Mn^{2+}, and anti-Beclin 1 Dz, utilizing BSA as a stabilizer. This nanomedicine exhibited straightforward preparation, high drug loading capacity, and responsive drug release, accumulating in tumor tissues and selectively targeting liver cancer cells. Upon cellular uptake, the nanoparticles disassembled, releasing their active constituents. Mn^{2+} activated Dz to cleave Beclin 1, inhibiting autophagy and promoting ATO-induced pyroptosis, thereby directly eliminating tumor cells. Additionally, the nanoparticles displayed remarkable targeting specificity, with 9 times greater cytotoxicity against tumor cells compared to normal cells, owing to the overexpression of folate receptors and GSDME proteins in tumor cells. Furthermore, pyroptosis induced ICD, activating antitumor immunity characterized by tumor antigen release, dendritic cell maturation, T cell infiltration and activation, and pro-inflammatory cytokine secretion. In preclinical models, the nanomedicine exhibited potent anti-tumor activity, achieving complete tumor growth inhibition and 100% survival at 45 days. Importantly, the nanoparticles demonstrated excellent biocompatibility and safety profiles, underscoring their potential for clinical translation. Our findings highlight the promise of nanotechnology-based strategies for precise cancer therapy and advocate for further exploration of the clinical application of our nanomedicine in cancer treatment.

Acknowledgements

This work was supported by the National Natural Science Foundation of China (82202398, 82270185), Research Foundation of Education Bureau of Hunan Province, China (23A0002), Hunan Provincial Natural Science Foundation of China (2025JJ60525, 2022JJ30903), China Postdoctoral Science Foundation (2023M733979), Health Research Project of Hunan Provincial Health Commission (W20243126, W20242008, China), and The "co-PI" project from The Third Xiangya hospital of Central South University (No. 202425, China).

Author contributions

Shengmei Wang: writing− original draft, methodology, investigation, data curation. Ding Ma: formal analysis, data curation. Minghua Yang: investigation. Ye Zhang: investigation. Shengfeng Wang: writing−original draft, supervision, project administration, funding acquisition, conceptualization. Wenhu Zhou: revising-original draft, visualization, supervision, project administration, conceptualization.

Conflicts of interest

The authors declare no conflicts of interest.

Appendix A. Supporting information

Supporting information to this article can be found online at https://doi.org/10.1016/j.apsb.2025.08.003.

References

1. Chi XQ, Liu K, Luo XJ, Yin ZY, Lin HY, Gao JH. Recent advances of nanomedicines for liver cancer therapy. *J Mater Chem B* 2020;**8**: 3747−71.
2. Anwanwan D, Singh SK, Singh S, Saikam V, Singh R. Challenges in liver cancer and possible treatment approaches. *Biochim Biophys Acta Rev Cancer* 2020;**1873**:188314.
3. Luo XT, He X, Zhang XM, Zhao XH, Zhang YZ, Shi YS, et al. Hepatocellular carcinoma: signaling pathways, targeted therapy, and immunotherapy. *MedComm* 2024;**5**:e474.
4. Gilles H, Garbutt T, Landrum J. Hepatocellular carcinoma. *Crit Care Nurs Clin* 2022;**34**:289−301.
5. Dimitroulis D, Damaskos C, Valsami S, Davakis S, Garmpis N, Spartalis E, et al. From diagnosis to treatment of hepatocellular carcinoma: an epidemic problem for both developed and developing world. *World J Gastroenterol* 2017;**23**:5282−94.
6. Dewhirst MW, Secomb TW. Transport of drugs from blood vessels to tumour tissue. *Nat Rev Cancer* 2017;**17**:738−50.
7. Huang C, Xie T, Liu YF, Yan S, OuYang FJ, Zhang HT, et al. A sodium alginate-based multifunctional nanoplatform for synergistic chemo-immunotherapy of hepatocellular carcinoma. *Adv Mater* 2023; **35**:e2301352.
8. Ji GF, Ma LS, Yao HC, Ma S, S XH, Wang YL, et al. Precise delivery of obeticholic acid *via* nanoapproach for triggering natural killer T cell-mediated liver cancer immunotherapy. *Acta Pharm Sin B* 2020; **10**:2171−82.

9. Mohamed MS, Bishr MK, Almutairi FM, Ali AG. Inhibitors of apoptosis: clinical implications in cancer. *Apoptosis* 2017;**22**: 1487−509.
10. Devarajan E, Sahin AA, Chen JS, Krishnamurthy RR, Aggarwal N, Brun AM, et al. Down-regulation of caspase 3 in breast cancer: a possible mechanism for chemoresistance. *Oncogene* 2002;**21**:8843−51.
11. Ma XB, Su W, Ye MJ, Gao Y, Qiu W, Liang MY, et al. Endogenous/exogenous stimulies inspired polyprodrug nano-inducer switches pyroptosis path for promoting antitumor immunity. *Nano Today* 2023; **48**:101727.
12. Chen BL, Yan Y, Yang Y, Cao G, Wang X, Wang YQ, et al. A pyroptosis nanotuner for cancer therapy. *Nat Nanotechnol* 2022;**17**: 788−98.
13. Wang FS, Fan YL, Liu Y, Lou XX, Sutrisno L, Peng SJ, et al. Oxygen-carrying semiconducting polymer nanoprodrugs induce sonopyroptosis for deep-tissue tumor treatment. *Explorations* 2024;**4**: 20230100.
14. Broz P, Pelegrín P, Shao F. The gasdermins, a protein family executing cell death and inflammation. *Nat Rev Immunol* 2020;**20**: 143−57.
15. Hsu SK, Li CY, Lin IL, Syue WJ, Chen YF, Cheng KC, et al. Inflammation-related pyroptosis, a novel programmed cell death pathway, and its crosstalk with immune therapy in cancer treatment. *Theranostics* 2021;**11**:8813−35.
16. He ZX, Feng DX, Zhang CJ, Chen ZQ, Wang H, Hou JQ, et al. Recent strategies for evoking immunogenic pyroptosis in antitumor immunotherapy. *J Control Release* 2024;**366**:375−94.
17. Peng ZYF, Wang PF, Song W, Yao QM, Li YJ, Liu LL, et al. GSDME enhances cisplatin sensitivity to regress non-small cell lung carcinoma by mediating pyroptosis to trigger antitumor immunocyte infiltration. *Signal Transduct Targeted Ther* 2020;**5**:159−61.
18. Wang QY, Wang YP, Ding JJ, Wang CH, Zhou XH, Gao WQ, et al. A bioorthogonal system reveals antitumour immune function of pyroptosis. *Nature* 2020;**579**:421−6.
19. Wang YP, Gao WQ, Shi XY, Ding JJ, Liu W, He HB, et al. Chemotherapy drugs induce pyroptosis through caspase-3 cleavage of a gasdermin. *Nature* 2017;**547**:99−103.
20. Jiang MX, Qi L, Li LS, Li YJ. The caspase-3/GSDME signal pathway as a switch between apoptosis and pyroptosis in cancer. *Cell Death Discov* 2020;**6**:112.
21. Kondo Y, Kanzawa T, Sawaya R, Kondo S. The role of autophagy in cancer development and response to therapy. *Nat Rev Cancer* 2005;**5**: 726−34.
22. Mohammad RM, Muqbil I, Lowe L, Yedjou C, Hsu HY, Lin LT, et al. Broad targeting of resistance to apoptosis in cancer. *Semin Cancer Biol* 2015;**35**:S78−103.
23. Yu P, Wang HY, Tian M, Li AX, Chen XS, Wang XL, et al. Eukaryotic elongation factor-2 kinase regulates the cross-talk between autophagy and pyroptosis in doxorubicin-treated human melanoma cells *in vitro*. *Acta Pharmacol Sin* 2019;**40**:1237−44.
24. Shi CS, Shenderov K, Huang NN, Kabat J, Abu-Asab M, Fitzgerald KA, et al. Activation of autophagy by inflammatory signals limits IL-1β production by targeting ubiquitinated inflammasomes for destruction. *Nat Immunol* 2012;**13**:255−63.
25. Li XY, Sun DL, Zhao TH, Zhang ZZ. Long non-coding RNA ROR confers arsenic trioxide resistance to HepG2 cells by inhibiting p53 expression. *Eur J Pharmacol* 2020;**872**:172982.
26. Chen S, Wu JL, Liang Y, Tang YG, Song HX, Wu LL, et al. Arsenic trioxide rescues structural p53 mutations through a cryptic allosteric site. *Cancer Cell* 2021;**39**:225−39.
27. Li X, Pan YF, Chen YB, Wan QQ, Lin YK, Shang TY, et al. Arsenic trioxide augments immunogenic cell death and induces cGAS−STING−IFN pathway activation in hepatocellular carcinoma. *Cell Death Dis* 2024;**15**:300.
28. Chen JF, Jin ZQ, Zhang SQ, Zhang X, Li PP, Yang H, et al. Arsenic trioxide elicits prophylactic and therapeutic immune responses against solid tumors by inducing necroptosis and ferroptosis. *Cell Mol Immunol* 2023;**20**:51−64.
29. Hu J, Dong Y, Ding L, Dong Y, Wu ZH, Wang WP, et al. Local delivery of arsenic trioxide nanoparticles for hepatocellular carcinoma treatment. *Signal Transduct Targeted Ther* 2019;**4**:28.
30. Swindell EP, Hankins PL, Chen HM, Miodragović DU, O'Halloran TV. Anticancer activity of small-molecule and nanoparticulate arsenic(III) complexes. *Inorg Chem* 2013;**52**:12292−304.
31. Sönksen M, Kerl K, Bunzen H. Current status and future prospects of nanomedicine for arsenic trioxide delivery to solid tumors. *Med Res Rev* 2022;**42**:374−98.
32. Yu MZ, Zhang YW, Fang MR, Jehan S, Zhou WH. Current advances of nanomedicines delivering arsenic trioxide for enhanced tumor therapy. *Pharmaceutics* 2022;**14**:743.
33. Chen Hm, MacDonald RC, Li Sy, Krett NL, Rosen ST, O'Halloran TV. Lipid encapsulation of arsenic trioxide attenuates cytotoxicity and allows for controlled anticancer drug release. *J Am Chem Soc* 2006;**128**:13348−9.
34. Zhai YH, Liu M, Yang T, Luo J, Wei CG, Shen JK, et al. Self-activated arsenic manganite nanohybrids for visible and synergistic thermo/immuno-arsenotherapy. *J Control Release* 2022;**350**:761−76.
35. Wang H, Zhang L, Miao ZH, Zhang M, Liu H, He Q, et al. PSMA-targeted arsenic nanosheets: a platform for prostate cancer therapy *via* ferroptosis and ATM deficiency-triggered chemosensitization. *Mater Horiz* 2021;**8**:2216−29.
36. Cui ZF, Zhang Y, Xia K, Yan QL, Kong HT, Zhang JC, et al. Nanodiamond autophagy inhibitor allosterically improves the arsenical-based therapy of solid tumors. *Nat Commun* 2018;**9**:4347.
37. Wang SM, Liu XJ, Wang SF, Ouyang LQ, Li H, Ding JS, et al. Imatinib co-loaded targeted realgar nanocrystal for synergistic therapy of chronic myeloid leukemia. *J Control Release* 2021;**338**:190−200.
38. Wang M, Song J, Zhou FF, Hoover AR, Murray C, Zhou BQ, et al. NIR-triggered phototherapy and immunotherapy *via* an antigen-capturing nanoplatform for metastatic cancer treatment. *Adv Sci* 2019;**6**:1802157.
39. Shi JJ, Gao WQ, Shao F. Pyroptosis: gasdermin-mediated programmed necrotic cell death. *Trends Biochem Sci* 2017;**42**:245−54.
40. Islam MA, Sooro MA, Zhang PH. Autophagic regulation of p62 is critical for cancer therapy. *Int J Mol Sci* 2018;**19**:1405.
41. Kanzawa T, Kondo Y, Ito H, Kondo S, Germano I. Induction of autophagic cell death in malignant glioma cells by arsenic trioxide. *Cancer Res* 2003;**63**:2103−8.
42. Zeng C, Zhang ZX, Luo W, Wang LY, Zhou H, Nie CL. JNK initiates Beclin-1 dependent autophagic cell death against Akt activation. *Exp Cell Res* 2022;**414**:113105.
43. Zhang ZW, Zhang H, Li DB, Zhou XP, Qin Q, Zhang QY. Caspase-3-mediated GSDME induced pyroptosis in breast cancer cells through the ROS/JNK signalling pathway. *J Cell Mol Med* 2021;**25**:8159−68.
44. Ju XL, Zhang H, Wang JY, Sun ZH, Guo LF, Wang Q. Shikonin triggers GSDME-mediated pyroptosis in tumours by regulating autophagy *via* the ROS-MAPK14/p38α axis. *Phytomedicine* 2023;**109**: 154596.
45. Yu JH, Li S, Qi J, Chen ZL, Wu YH, Guo J, et al. Cleavage of GSDME by caspase-3 determines lobaplatin-induced pyroptosis in colon cancer cells. *Cell Death Dis* 2019;**10**:193.
46. Kimura T, Takabatake Y, Takahashi A, Isaka Y. Chloroquine in cancer therapy: a double-edged sword of autophagy. *Cancer Res* 2013;**73**: 3−7.
47. Liu P, Liu XJ, Cheng Y, Zhong SH, Shi XY, Wang SF, et al. Core-shell nanosystems for self-activated drug-gene combinations against triple-negative breast cancer. *ACS Appl Mater Interfaces* 2020;**12**: 53654−64.
48. Zhou WH, Saran R, Liu JW. Metal sensing by DNA. *Chem Rev* 2017; **117**:8272−325.
49. Zhou WH, Ding JS, Liu JW. Theranostic DNAzymes. *Theranostics* 2017;**7**:1010−25.
50. Guo J, Liu P, Wei BL, Peng Y, Ding JS, Zhang HL, et al. Reversing the negative effect of adenosine A1 receptor-targeted immunometabolism modulation on melanoma by a co-delivery nanomedicine for self-activation of anti-PD-L1 DNAzyme. *Nano Today* 2023;**48**:101722.

51. Zhu JJ, Chang RM, Wei BL, Fu Y, Chen X, Liu H, et al. *Photothermal nano-vaccine promoting antigen presentation and dendritic cells infiltration for enhanced immunotherapy of melanoma via transdermal microneedles delivery*, **2022**. Research (Wash D C); 2022. p. 9816272.
52. Liu P, Shi XY, Peng Y, Hu JM, Ding JS, Zhou WH. Anti-PD-L1 DNAzyme loaded photothermal Mn^{2+}/Fe^{3+} hybrid metal-phenolic networks for cyclically amplified tumor ferroptosis-immunotherapy. *Adv Healthcare Mater* 2022;**11**:e2102315.
53. Zhang ZB, Zhang Y, Xia SY, Kong Q, Li SY, Liu X, et al. Gasdermin E suppresses tumour growth by activating anti-tumour immunity. *Nature* 2020;**579**:415−20.
54. Qiu W, Su W, Xu JM, Liang MY, Ma XB, Xue P, et al. Immunomodulatory-photodynamic nanostimulators for invoking pyroptosis to augment tumor immunotherapy. *Adv Healthcare Mater* 2022;**11**:e2201233.
55. Obeid M, Panaretakis T, Joza N, Tufi R, Tesniere A, Endert PV, et al. Calreticulin exposure is required for the immunogenicity of gamma-irradiation and UVC light-induced apoptosis. *Cell Death Differ* 2007;**14**:1848−50.
56. Martins I, Tesniere A, Kepp O, Michaud M, Schlemmer F, Senovilla L, et al. Chemotherapy induces ATP release from tumor cells. *Cell Cycle* 2009;**8**:3723−8.
57. Ding D, Jiang XQ. Advances in Immunogenic Cell death for cancer immunotherapy. *Small Methods* 2023;**7**:e2300354.
58. Ge Y, Huang M, Yao YM. The effect and regulatory mechanism of high mobility group box-1 protein on immune cells in inflammatory diseases. *Cells* 2021;**10**:1044.